



HAL
open science

Sliding and merging of strongly sheared droplets

C Ruyer-Quil, D Bresch, M Gisclon, G L Richard, M Kessar, Nicolas Cellier

► **To cite this version:**

C Ruyer-Quil, D Bresch, M Gisclon, G L Richard, M Kessar, et al.. Sliding and merging of strongly sheared droplets. 2023. hal-04193284v1

HAL Id: hal-04193284

<https://hal.science/hal-04193284v1>

Preprint submitted on 1 Sep 2023 (v1), last revised 2 Nov 2023 (v2)

HAL is a multi-disciplinary open access archive for the deposit and dissemination of scientific research documents, whether they are published or not. The documents may come from teaching and research institutions in France or abroad, or from public or private research centers.

L'archive ouverte pluridisciplinaire **HAL**, est destinée au dépôt et à la diffusion de documents scientifiques de niveau recherche, publiés ou non, émanant des établissements d'enseignement et de recherche français ou étrangers, des laboratoires publics ou privés.

Copyright

Sliding and merging of strongly sheared droplets

C. Ruyer-Quil ¹†, D. Bresch ², M. Gisclon ², G. L. Richard ³, M. Kessar ² and N. Cellier ⁴

¹Université Savoie Mont Blanc, CNRS UMR 5271, LOCIE, 73376 Chambéry, France

²Université Savoie Mont Blanc, CNRS UMR 5127, LAMA, 73376 Chambéry, France

³Univ. Grenoble Alpes, INRAE, IGE, Grenoble, France

⁴IMT, Mines d'Albi, 81 000 Albi, France

(Received xx; revised xx; accepted xx)

A mathematical and numerical framework is proposed to compute the displacement and merging dynamics of sliding droplets under the action of a constant shear exerted by a gas flow. An augmented formulation is implemented to model surface tension including the full curvature of the free surface. A set of shallow-water evolution equations for the film thickness, the averaged velocity, an additional quantity (with dimension of a velocity) taking into account the capillary effects, and a tensor called *enstrophy*, is obtained. The enstrophy accounts for the deviation of the velocity profile from a constant velocity distribution. The formulation is consistent with the long-wave expansion of the basic equations with a conservative part and source terms including the effect of viscosity, in the form of a viscous friction, and the effect of the shear stress. The model is hyperbolic with generalized diffusion terms due to capillarity. Finally, our model is completed with a disjoining pressure formulation that is able to account for the hysteresis of the static contact angle. In this formulation, the advancing or receding nature of the contact line is assessed by the accumulation or reduction of mass of the droplet at the contact line. Simulations of sliding water droplets are performed with periodic boundary conditions in a domain of limited size. Hysteresis of the static contact angle causes a slowdown of the drops and a delay in the sequence of coalescence of the drops.

1 Introduction

Transport of water droplets or films at the surface on a rigid wall under the action of a shear exerted by the surrounding atmosphere (shear flow) is drawing an increasing attention due to its importance in aeronautics in the context of icing phenomena.

Some experimental studies describe the phenomenon of shedding, which is the detachment of sessile droplet induced by the gas flow, and considered either the effect of the presence of other droplets (Razzaghi & Amirfazli 2019) or the influence of the surface wettability (Milne & Amirfazli 2009; Fan *et al.* 2011). Fan *et al.* (2011) observed that the droplet may retain a footprint similar to that at the point of motion, or exhibit a tail. In some cases, a trail remains behind the droplet (that can shed smaller droplets). In the context of aerodynamic applications, Moghtadernejad *et al.* (2016) further consider the coalescence of identical water droplets, on an aluminium plate. Their study reveals the formation of a rivulet as the result of the coalescence process. These authors further considered the evolution of rivulets on substrates of different wettabilities sheared by a high-velocity air stream (Moghtadernejad & Dolatabadi 2014).

† Email address for correspondence: ruyerc@univ-smb.fr

42 In the context of the wind-driven water run-back process on an airfoil, (Zhang *et al.*
 43 2015; Zhang & Hu 2016) considered the formation of water rivulets on a NACA0012
 44 airfoil. The rivulets width and rivulets distributions along the wing span were found to
 45 depend on the airflow velocity and to result from the destabilization of the liquid film
 46 which forms at the leading edge of the air foil. The instability mechanism is related to
 47 the dynamics of the advancing contact line during the water film run-back.

48 In most cases, numerical studies focus on the averaged properties of the film (liquid
 49 hold-up) and did not resolve the wavy nature of the liquid interface (see for instance
 50 Lan *et al.* (2008)). However, some recent studies have been proposed based on crude low-
 51 dimensional modeling of the film flow yielding conservative, hyperbolic and two-dimen-
 52 sional equations (Gosset 2017; Lallement *et al.* 2018). Gosset (2017) used the numerical
 53 framework proposed by Meredith *et al.* (2011) which is based on a VOF formulation
 54 and the Continuum Surface Force model (CSF) introduced by Brackbill *et al.* (1992).
 55 Using OPENFOAM software, her simulations reproduced quite satisfactorily the onset
 56 of rivulets observed by Zhang *et al.* (2015); Zhang & Hu (2016). However, reasonable
 57 comparisons are impaired by the dependency of the results on the parameters of the
 58 partial-wetting model. Besides, the curvature of the interface is linearised using the long-
 59 wave approximation in this study.

60 Lallement *et al.* (2018) proposed instead to model surface tension with an augmented
 61 formulation. They introduced a transport equation for the gradient of the film thickness,
 62 $\mathbf{p} = \mathbf{grad} h$. This formulation enables to lower the order of the derivatives in the averaged
 63 momentum balance from third-order to second-order. Such an augmented formulation
 64 has been initially proposed in Bresch *et al.* (2016) but limited to the linearised long-
 65 wave approximation of the curvature of the free surface. They also introduced an
 66 innovative approach of partial wetting within the framework of the disjoining pressure
 67 model proposed by Derjaguin (1940). A literature review of the different formulations of
 68 disjoining pressure to model long-range surface forces within the framework of long-wave
 69 thin-film equations is available in Oron *et al.* (1997). Lallement *et al.* thus introduced a
 70 disjoining force accounts for partial wetting and enables to regularize the discontinuity
 71 of surface energy at the contact line at a scale h_* , which corresponds physically to the
 72 range of microscopic forces, but is taken much larger at the order of the mesh size. The
 73 evolution equations derived by Lallement *et al.* is compatible with a conservation law of
 74 the total energy of the equation at the macroscopic level. However, a discretization which
 75 preserves this property at the discrete level has not been achieved yet (Lallement 2019).

76 Within the framework of long-wave approximation, the Derjaguin disjoining pressure
 77 model has been used extensively to simulate the spreading and sliding of droplets
 78 (Bertozzi & Pugh 1994; Brandon *et al.* 1997; Schwartz & Eley 1998; Ahmed *et al.* 2014;
 79 Espín & Kumar 2017) as well as the fingering instability of a liquid film front (Zhao
 80 & Marshall 2006). One advantage of the Derjaguin formulation is the introduction of a
 81 precursor film which alleviates the divergence of the viscous stresses at the contact line,
 82 also known as 'the contact-line paradox' (Dussan 1979). Precursor films are known to be
 83 observable for static and spreading non-volatile droplets and emerge from the absorption
 84 of the liquid at the solid surface by long-range forces such as van der Waals forces. Typical
 85 measured thicknesses of precursor films are 0 (100 Å) (Popescu *et al.* 2012).

86 An alternative to this approach is the assumption of a slip at the wall boundary
 87 (see e.g. Haley & Miksis (1991); Savva & Kalliadasis (2009)). This approach is justified
 88 by molecular dynamics simulations (Ren & E 2007). The two approaches have been
 89 compared by Diez & Bertozzi (2000) who reported that much lower values of the slip
 90 length than the precursor film thickness are required to capture satisfactorily the moving
 91 contact line characteristics, either speed or shape. Besides, the precursor film formulation

92 does not require to track the contact line location. The Derjaguin approach has been
 93 employed by [Ahmed *et al.* \(2014\)](#) to study the sliding of drops. Their formulation adjusted
 94 the Hamacker constant of the disjoining pressure at the front of the rear of the drops,
 95 to prescribe an advancing and a receding contact angles. Indeed, a hysteresis of the
 96 static contact angles at the advancing and receding fronts may be observed as a result
 97 of the surface inhomogeneities ([Schwartz & Eley 1998](#); [Zhao & Marshall 2006](#)), either
 98 roughness ([Savva & Kalliadasis 2009](#)) or chemical heterogeneities of the surface ([Brandon
 99 *et al.* 1997](#)), or the presence of solutes (polymers or surfactants) in the liquid which
 100 may contaminate the surface and form a film ([de Gennes 1985](#)). Typical contact angle
 101 hysteresis is 10° ([de Gennes 1985](#)) but may be higher. This phenomenon generates the
 102 adhesion force of a sessile droplet and determines the onset of shedding ([Mahé *et al.*
 103 1988](#); [Milne & Amirfazli 2009](#); [Moghtadernejad & Dolatabadi 2014](#)), as well as the speed
 104 and shape of sliding droplets on an inclined plane ([Ahmed *et al.* 2014](#)).

105 In this paper, we wish to formulate a set of averaged equations which models the
 106 evolution of a gas liquid film sheared by a gas flow within the framework of the shallow-
 107 water equations, which is well adapted for large Reynolds number flows. This approach
 108 enables us to depart from the usual creeping flow assumption used in lubrication theory,
 109 as in [Espín & Kumar \(2017\)](#) for instance, which is not valid for typical experimental
 110 conditions of shear-driven droplets. As an example, [Fan *et al.* \(2011\)](#) conducted exper-
 111 iments of water, water-glycerin and glycerin droplets of typical thickness which can be
 112 estimated to be $h \approx 1$ mm, sheared by an air flow in a wind tunnel of effective parameter
 113 $L_{\text{eff}} = 0.032$ m. They reported typical gas velocities of $V_a \approx 10$ m/s. With the help of
 114 the correlation

$$\frac{2\rho_a\tau_e}{V_a^2} = 0.0792Re_G^{-1/4} \quad (1.1)$$

115 where the gas Reynolds number defined as $Re_G = V_a L_{\text{eff}}/\mu_a$. This gives $\tau_e \approx 0.4$ Pa and
 116 consequently a liquid Reynolds number $Re \approx 400$ for water, in which case the creeping
 117 flow assumption is no more admissible.

118 Besides, our formulation is based on an augmented formulation proposed by [Bresch
 119 *et al.* \(2020\)](#) which enables to avoid the long-wave approximation of the free-surface
 120 curvature, a questionable assumption for large contact angles.

121 Our formulation alleviates the limitations of previous attempts by conserving the sur-
 122 face and disjoining energy and preserving the consistency with the long wave asymptotics.
 123 This proposed derivation will account for the displacement of contact lines with the
 124 Derjaguin formula. The evolution of droplets under the action of a flow is investigated.
 125 In particular, we are interested in the effect of the contact angle hysteresis on the droplets
 126 speed and shape. In this work, we limit ourselves to consider only a constant external
 127 shear stress. For a boundless gas flow, this assumption is admissible as long as the wake
 128 of the droplet does not generate a boundary-layer separation in the gas flow. Indeed,
 129 the shear stress exerted by the gas flow is determined by the boundary layer at the gas-
 130 liquid interface. Since, boundary-layer equations obey to the Prandtl transformation, the
 131 response of the shear stress to the wall geometry is negligible as long as the potential flow
 132 far from the wall remains unaffected. For open flows, wall roughness thus only affect the
 133 wall shear stress through second-order modifications of the pressure in the outer potential
 134 region ([Luchini & Charru 2019](#)).

135 Section 2 is devoted to the mathematical formulation that is able to describe the
 136 sliding of the drops under a constant shear. This mathematical framework is based on
 137 the Saint-Venant approach, i.e. an in-depth averaging of the basic equations which is
 138 made possible by the long-wave nature of the flow as the typical thickness of the water

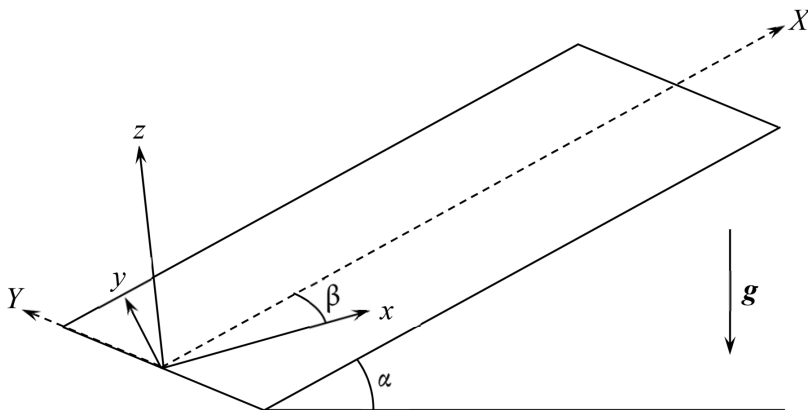


Figure 1: Definition sketch.

139 layer is much smaller than the extension of the drop on the wall. Section 3 presents
 140 a numerical investigation of the characteristics of single droplets and the coalescence
 141 dynamics of a cloud of small droplets in a periodic domain. Concluding remarks are
 142 given in § 4.

143 2 Mathematical developments

144 2.1 Governing equations

145 We consider an incompressible Newtonian fluid of dynamic viscosity μ , density ρ and
 146 surface tension γ . The kinematic viscosity is denoted by ν . We study the propagation
 147 of a droplet upward on an inclined plane under the action of a constant shear stress
 148 of intensity τ_e . The inclination angle is denoted by α . The Ox -axis is oriented upward
 149 with an angle β with the line of the greatest slope OX and the Oz -axis is normal to the
 150 plane. Finally, the Oy -axis is chosen to form a direct orthonormal basis (see Figure 1).
 151 The liquid depth (in the Oz -direction) is denoted by h . The equations are written in the
 152 reference frame of the plane, which is supposed to be Galilean. The gas is supposed to
 153 impose a constant pressure and a constant shear stress. The fluid velocity \mathbf{v} satisfies the
 154 continuity equation

$$\operatorname{div} \mathbf{v} = 0. \quad (2.1)$$

155 Denoting by $\boldsymbol{\tau}$ the viscous stress tensor and by p the pressure, the Navier-Stokes equation
 156 writes

$$\rho \left[\frac{\partial \mathbf{v}}{\partial t} + \operatorname{div} (\mathbf{v} \otimes \mathbf{v}) \right] = \rho \mathbf{g} - \operatorname{grad} p + \operatorname{div} \boldsymbol{\tau} \quad (2.2)$$

where \mathbf{g} is the weight acceleration and \otimes the tensor product. The constitutive relation
 is $\boldsymbol{\tau} = 2\mu \mathbf{D}$ where \mathbf{D} is the strain rate tensor defined by

$$\mathbf{D} = (1/2)[\operatorname{grad} \mathbf{v} + (\operatorname{grad} \mathbf{v})^T].$$

157 The components of the velocity are denoted by u , v and w respectively in the Ox , Oy
158 and Oz -directions and the components of the tensor $\boldsymbol{\tau}$ are denoted by

$$\boldsymbol{\tau} = \begin{pmatrix} \tau_{xx} & \tau_{xy} & \tau_{xz} \\ \tau_{xy} & \tau_{yy} & \tau_{yz} \\ \tau_{xz} & \tau_{yz} & \tau_{zz} \end{pmatrix} \quad (2.3)$$

159 Note that the continuity equation implies that $\tau_{zz} = -\tau_{xx} - \tau_{yy}$.

At the bottom, the no-slip and no-penetration boundary conditions hold

$$\mathbf{v}(0) = 0.$$

160 At the free surface, the kinematic boundary condition can be written

$$\frac{\partial h}{\partial t} + u(h) \frac{\partial h}{\partial x} + v(h) \frac{\partial h}{\partial y} = w(h) \quad (2.4)$$

161 The dynamic boundary condition at the free surface gives three scalar equations, which
162 are

$$\tau_{xz}(h) + [p(h) - \tau_{xx}(h)] \frac{\partial h}{\partial x} - \tau_{xy}(h) \frac{\partial h}{\partial y} + \gamma \frac{\partial h}{\partial x} K = \tau_{ex}, \quad (2.5)$$

163

$$\tau_{yz}(h) + [p(h) - \tau_{yy}(h)] \frac{\partial h}{\partial y} - \tau_{xy}(h) \frac{\partial h}{\partial x} + \gamma \frac{\partial h}{\partial y} K = \tau_{ey}, \quad (2.6)$$

164

$$p(h) + \tau_{xz}(h) \frac{\partial h}{\partial x} + \tau_{yz}(h) \frac{\partial h}{\partial y} - \tau_{zz}(h) + \gamma K = \tau_{ex} \frac{\partial h}{\partial x} + \tau_{ey} \frac{\partial h}{\partial y}. \quad (2.7)$$

165 In these equations and in the following, K denotes the total curvature

$$K = \operatorname{div} \frac{\mathbf{grad} h}{\sqrt{1 + \mathbf{grad} h \cdot \mathbf{grad} h}} \quad (2.8)$$

166 and τ_{ex} , τ_{ey} are the components in the Ox and Oy -directions respectively of the shear
167 stress $\boldsymbol{\tau}_e$ imposed on the free surface. In the following, this shear stress is supposed to
168 be a constant.

169

2.2 Scaling

170 The equations are derived with several assumptions concerning the order of magnitude
171 of the dimensionless parameters of the problem. The shallow water parameter is supposed
172 to be a small parameter so that

$$\varepsilon = \frac{h_0}{L} \ll 1 \quad (2.9)$$

173 where h_0 is the characteristic depth and L the characteristic length in the Ox and Oy -
174 directions. The order of magnitude of all other dimensionless parameters will be defined
175 by comparison with ε . The imposed shear stress at the free surface is large compared to
176 the hydrostatic pressure. More precisely, we suppose that

$$\delta = \frac{\rho g h_0}{\tau_e} = O(\varepsilon^2). \quad (2.10)$$

177 The characteristic velocity is defined from the imposed shear stress at the surface as

$$u_0 = \frac{h_0 \tau_e}{\mu}. \quad (2.11)$$

178 The Reynolds number defined with this velocity and with the characteristic fluid depth
179 is supposed to be of $O(1)$ i.e.

$$Re = \frac{h_0 u_0}{\nu} = \frac{\rho h_0^2 \tau_e}{\mu^2} = O(1). \quad (2.12)$$

180 The Weber number is defined by

$$We = \frac{\rho h_0 u_0^2}{\gamma} = \frac{\rho h_0^3 \tau_e^2}{\gamma \mu^2} = O(\varepsilon^2). \quad (2.13)$$

181 It will be convenient to use the number

$$\kappa = \frac{\varepsilon^2}{We} = O(1) \quad (2.14)$$

182 which is of $O(1)$. The angle α is such that $\sin \alpha = O(1)$ and the same assumption is made
183 for β , although the equations will be used in practice most of the time with $\beta = 0$. We will
184 keep a non-zero value for β in all the derivation process, so that the final equations do not
185 depend on the particular orientation of the axes. We define the following dimensionless
186 numbers

$$\lambda_x = \frac{\delta \sin \alpha \cos \beta}{Re} = \varepsilon^2 \lambda_1, \quad \lambda_y = \frac{\delta \sin \alpha \sin \beta}{Re} = \varepsilon^2 \lambda_2, \quad \lambda_z = \frac{\delta \cos \alpha}{Re} = \varepsilon^2 \lambda_3, \quad (2.15)$$

187 where λ_1 , λ_2 and λ_3 are of $O(1)$. The dimensionless quantities (denoted with a tilde) are
188 defined with the following scaling

$$\begin{aligned} \tilde{u} &= \frac{u}{u_0} = \frac{\mu u}{h_0 \tau_e}, & \tilde{v} &= \frac{v}{u_0} = \frac{\mu v}{h_0 \tau_e}, & \tilde{w} &= \frac{u_0}{\varepsilon u_0} = \frac{\mu w}{\varepsilon h_0 \tau_e}, \\ \tilde{x} &= \frac{x}{L}, & \tilde{y} &= \frac{y}{L}, & \tilde{z} &= \frac{z}{h_0}, & \tilde{h} &= \frac{h}{h_0}, & \tilde{t} &= \frac{u_0}{L} t = \frac{h_0 \tau_e}{\mu L} t, & \tilde{K} &= \frac{L}{\varepsilon} K, \\ \tilde{\tau}_{xz} &= \frac{\tau_{xz}}{\tau_e}, & \tilde{\tau}_{yz} &= \frac{\tau_{yz}}{\tau_e}, & \tilde{\tau}_{ex} &= \frac{\tau_{ex}}{\tau_e}, & \tilde{\tau}_{ey} &= \frac{\tau_{ey}}{\tau_e}, \\ \tilde{\tau}_{xy} &= \frac{\tau_{xy}}{\varepsilon \tau_e}, & \tilde{\tau}_{xx} &= \frac{\tau_{xx}}{\varepsilon \tau_e}, & \tilde{\tau}_{yy} &= \frac{\tau_{yy}}{\varepsilon \tau_e}, & \tilde{\tau}_{zz} &= \frac{\tau_{zz}}{\varepsilon \tau_e}. \end{aligned} \quad (2.16)$$

189 The pressure is dominated by the Laplace pressure and scaled accordingly

$$\tilde{p} = \frac{L^2}{\gamma h_0} p. \quad (2.17)$$

190 To lighten the notations, the tildes are now dropped. In dimensionless form, we can write
191 the mass conservation equation

$$\frac{\partial u}{\partial x} + \frac{\partial v}{\partial y} + \frac{\partial w}{\partial z} = 0 \quad (2.18)$$

192 and the momentum equation, in the Ox , Oy and Oz -directions respectively,

$$\frac{\partial u}{\partial t} + \frac{\partial u^2}{\partial x} + \frac{\partial uv}{\partial y} + \frac{\partial uw}{\partial z} = -\kappa \frac{\partial p}{\partial x} + \frac{\varepsilon}{Re} \frac{\partial \tau_{xx}}{\partial x} + \frac{\varepsilon}{Re} \frac{\partial \tau_{xy}}{\partial y} + \frac{1}{\varepsilon Re} \frac{\partial \tau_{xz}}{\partial z} - \varepsilon \lambda_1, \quad (2.19)$$

193

$$\frac{\partial v}{\partial t} + \frac{\partial uv}{\partial x} + \frac{\partial v^2}{\partial y} + \frac{\partial vw}{\partial z} = -\kappa \frac{\partial p}{\partial y} + \frac{\varepsilon}{Re} \frac{\partial \tau_{xy}}{\partial x} + \frac{\varepsilon}{Re} \frac{\partial \tau_{yy}}{\partial y} + \frac{1}{\varepsilon Re} \frac{\partial \tau_{yz}}{\partial z} - \varepsilon \lambda_2, \quad (2.20)$$

$$\begin{aligned} \varepsilon^2 \left[\frac{\partial w}{\partial t} + \frac{\partial uw}{\partial x} + \frac{\partial vw}{\partial y} + \frac{\partial w^2}{\partial z} \right] &= -\kappa \frac{\partial p}{\partial z} + \frac{\varepsilon}{Re} \frac{\partial \tau_{xz}}{\partial x} + \frac{\varepsilon}{Re} \frac{\partial \tau_{yz}}{\partial y} + \frac{\varepsilon}{Re} \frac{\partial \tau_{zz}}{\partial z} \\ &\quad - \varepsilon^2 \lambda_3. \end{aligned} \quad (2.21)$$

The boundary conditions at the bottom plane become $u(0) = v(0) = w(0) = 0$. The boundary conditions at the free surface can be written

$$w(h) = \frac{\partial h}{\partial t} + u(h) \frac{\partial h}{\partial x} + v(h) \frac{\partial h}{\partial y}$$

194 and

$$\tau_{xz}(h) + [\varepsilon \kappa Re p(h) - \varepsilon^2 \tau_{xx}(h)] \frac{\partial h}{\partial x} - \varepsilon^2 \tau_{xy}(h) \frac{\partial h}{\partial y} + \varepsilon \kappa Re \frac{\partial h}{\partial x} K = \tau_{ex}, \quad (2.22)$$

195

$$\tau_{yz}(h) + [\varepsilon \kappa Re p(h) - \varepsilon^2 \tau_{yy}(h)] \frac{\partial h}{\partial y} - \varepsilon^2 \tau_{xy}(h) \frac{\partial h}{\partial x} + \varepsilon \kappa Re \frac{\partial h}{\partial y} K = \tau_{ey}, \quad (2.23)$$

$$\begin{aligned} p(h) + \frac{\varepsilon}{\kappa Re} \tau_{xz}(h) \frac{\partial h}{\partial x} + \frac{\varepsilon}{\kappa Re} \tau_{yz}(h) \frac{\partial h}{\partial y} - \frac{\varepsilon}{\kappa Re} \tau_{zz}(h) + K \\ = \frac{\varepsilon}{\kappa Re} \tau_{ex} \frac{\partial h}{\partial x} + \frac{\varepsilon}{\kappa Re} \tau_{ey} \frac{\partial h}{\partial y}. \end{aligned} \quad (2.24)$$

196 Finally the constitutive relation leads to

$$\begin{aligned} \tau_{xy} = \frac{\partial u}{\partial y} + \frac{\partial v}{\partial x}; \quad \tau_{xz} = \frac{\partial u}{\partial z} + \varepsilon^2 \frac{\partial w}{\partial x}; \quad \tau_{yz} = \frac{\partial v}{\partial z} + \varepsilon^2 \frac{\partial w}{\partial y}; \\ \tau_{xx} = 2 \frac{\partial u}{\partial x}; \quad \tau_{yy} = 2 \frac{\partial v}{\partial y}; \quad \tau_{zz} = -\tau_{xx} - \tau_{yy}. \end{aligned} \quad (2.25)$$

197

2.3 Asymptotic expansions

198 To derive a consistent first-order model, accurate to within $O(\varepsilon^2)$, an asymptotic
199 method is used. The fields (velocity, pressure, viscous stress) are expanded as $X =$
200 $X^{(0)} + \varepsilon X^{(1)} + O(\varepsilon^2)$ where X refers to other $u, v, w, p, \tau_{xx}, \tau_{yy}, \tau_{zz}, \tau_{xz}, \tau_{yz}, \tau_{xy}$.

201 These expansions are inserted into the dimensionless equations of the flow to calculate
202 the fields at orders 0 and 1.

203 At order 0, the momentum equations (2.19) and (2.20) lead to

$$\frac{\partial \tau_{xz}^{(0)}}{\partial z} = 0; \quad \frac{\partial \tau_{yz}^{(0)}}{\partial z} = 0. \quad (2.26)$$

204 This gives $\tau_{xz}^{(0)} = \tau_{xz}^{(0)}(h)$ and $\tau_{yz}^{(0)} = \tau_{yz}^{(0)}(h)$. These expressions can be found from the
205 dynamic boundary conditions (2.22) and (2.23). At order 0, we have simply

$$\tau_{xz}^{(0)} = \tau_{ex}; \quad \tau_{yz}^{(0)} = \tau_{ey}. \quad (2.27)$$

206 Since we suppose that the imposed shear stress at the free surface is a constant, these
207 two components of the viscous stress tensor are uniform in the droplet at order 0. From
208 the constitutive relation (2.25) and the no-slip condition, we obtain the components $u^{(0)}$
209 and $v^{(0)}$

$$u^{(0)} = \tau_{ex} z; \quad v^{(0)} = \tau_{ey} z. \quad (2.28)$$

210 The linear profile of the velocity is characteristic of a planar Couette flow. The mass
211 conservation equation (2.18) enables to calculate $w^{(0)}$. Since $u^{(0)}$ and $v^{(0)}$ do not depend
212 on x or y , the integration is straightforward. Taken into account the no-penetration
213 boundary condition, we find $w^{(0)} = 0$. At order 0, the momentum equation (2.21)
214 reduces to $-K \partial p^{(0)} / \partial z = 0$. This implies that $p^{(0)} = p^{(0)}(h)$. At this order, the dynamic
215 boundary condition (2.24) is simply $p^{(0)}(h) = -K$, which gives

$$p^{(0)} = -K. \quad (2.29)$$

- 216** The pressure in the droplet is, at order 0, entirely determined by the Laplace pressure.
217 The remaining components of the viscous stress tensor are calculated from $u^{(0)}$, $v^{(0)}$ and
218 the constitutive relation (2.25). The result is simply

$$\tau_{xx}^{(0)} = 0; \quad \tau_{yy}^{(0)} = 0; \quad \tau_{zz}^{(0)} = 0; \quad \tau_{xy}^{(0)} = 0. \quad (2.30)$$

- 219** At order 1, the momentum equation (2.19) gives

$$\frac{\partial \tau_{xz}^{(1)}}{\partial z} = \kappa Re \frac{\partial p^{(0)}}{\partial x}. \quad (2.31)$$

- 220** This equation can be integrated together with the expression (2.29) of the pressure at
221 order 0 and the dynamic boundary condition (2.22), which writes at order 1

$$\tau_{xz}^{(1)}(h) = -\kappa Re p^{(0)}(h) \frac{\partial h}{\partial x} - \kappa Re \frac{\partial h}{\partial x} K = 0. \quad (2.32)$$

- 222** This leads to

$$\tau_{xz}^{(1)} = \kappa Re \frac{\partial K}{\partial x} (h - z), \quad \tau_{yz}^{(1)} = \kappa Re \frac{\partial K}{\partial y} (h - z). \quad (2.33)$$

- 223** The constitutive relation (2.25) gives at order 1

$$\frac{\partial u^{(1)}}{\partial z} = \tau_{xz}^{(1)}; \quad \frac{\partial v^{(1)}}{\partial z} = \tau_{yz}^{(1)}. \quad (2.34)$$

- 224** These equations can be integrated with the no-slip condition to obtain

$$u^{(1)} = \kappa Re \frac{\partial K}{\partial x} z \left(h - \frac{z}{2} \right); \quad v^{(1)} = \kappa Re \frac{\partial K}{\partial y} z \left(h - \frac{z}{2} \right). \quad (2.35)$$

- 225** It is not necessary to calculate $w^{(1)}$, $p^{(1)}$ or the other components of the viscous stress
226 tensor at order 1.

227 2.4 Depth-averaging procedure

228 2.4.1 Average velocity

- 229** The model is obtained by averaging over the depth the equations of the flow. For any
230 quantity A , its depth-averaged value is defined by

$$\langle A \rangle = \frac{1}{h} \int_0^h A \, dz. \quad (2.36)$$

Furthermore, we will use the notations $U = \langle u \rangle$; $V = \langle v \rangle$. It is necessary to expand also U and V as $U = U^{(0)} + \varepsilon U^{(1)} + O(\varepsilon^2)$, $V = V^{(0)} + \varepsilon V^{(1)} + O(\varepsilon^2)$. The expressions (2.28) and (2.35) enable to calculate

$$U^{(0)} = \frac{1}{2} \tau_{ex} h; \quad V^{(0)} = \frac{1}{2} \tau_{ey} h; \quad U^{(1)} = \kappa Re \frac{\partial K}{\partial x} \frac{h^2}{3}; \quad V^{(1)} = \kappa Re \frac{\partial K}{\partial y} \frac{h^2}{3}.$$

231 2.4.2 Mass and momentum equations

- 232** Integrating the mass conservation equation (2.18) together with the no-penetration
233 condition at the bottom and the kinematic boundary condition at the free surface leads
234 to the equation

$$\frac{\partial h}{\partial t} + \operatorname{div}(h\mathbf{U}) = 0 \quad (2.37)$$

- 235** where $\mathbf{U} = (U, V)^T$ is the depth-averaged velocity vector. The momentum equation (2.19)
236 in the Ox -direction is integrated over the depth, with the no-penetration condition and

237 the kinematic boundary condition, to obtain

$$\frac{\partial h U}{\partial t} + \frac{\partial h \langle u^2 \rangle}{\partial x} + \frac{\partial h \langle uv \rangle}{\partial y} + \kappa \int_0^h \frac{\partial p}{\partial x} dz = \frac{1}{\varepsilon Re} (\tau_{xz}(h) - \tau_{xz}(0)) + O(\varepsilon). \quad (2.38)$$

238 Note that the terms with the derivatives of the components τ_{xx} , τ_{xy} , τ_{yy} are negligible
 239 at this order of accuracy. This implies that there is no diffusive term due to the viscosity
 240 in the model, which, apart from the capillary terms, is hyperbolic. The effect of viscosity
 241 is represented by the terms with τ_{xz} , which give, by integration over the depth, a viscous
 242 friction and a driving force due to the shear at the free surface. In this equation, the
 243 pressure can be evaluated at order zero to calculate the integral

$$\kappa \int_0^h \frac{\partial p}{\partial x} dz = -\kappa h \frac{\partial K}{\partial x} + O(\varepsilon). \quad (2.39)$$

244 The right-hand side of (2.38) is evaluated with the expressions at order 0 (2.27) and order
 245 1 of τ_{xz} and with the expression of $U^{(1)}$:

$$\tau_{xz}(h) = \tau_{ex} + O(\varepsilon^2); \quad \tau_{xz}(0) = \tau_{ex} + \varepsilon \frac{3U^{(1)}}{h} + O(\varepsilon^2). \quad (2.40)$$

246 Since $U^{(1)}$ can be written

$$U^{(1)} = \frac{U - U^{(0)}}{\varepsilon} + O(\varepsilon), \quad (2.41)$$

247 Equation (2.38) can be written with a relaxation term as

$$\frac{\partial h U}{\partial t} + \frac{\partial h \langle u^2 \rangle}{\partial x} + \frac{\partial h \langle uv \rangle}{\partial y} = \frac{1}{\varepsilon Re} \left(\frac{3}{2} \tau_{ex} - \frac{3U}{h} \right) + \kappa h \frac{\partial K}{\partial x} + O(\varepsilon). \quad (2.42)$$

To calculate $\langle u^2 \rangle$, $\langle uv \rangle$ and thereafter $\langle v^2 \rangle$, u and v are expanded as

$$u = U + u'; \quad v = V + v'$$

248 where u' and v' are the deviations of u and v respectively with respect to their depth-
 249 averaged values U and V . Then $\langle u^2 \rangle = U^2 + \langle u'^2 \rangle$ since, by definition, $\langle u' \rangle = 0$. In vector
 250 form, the velocity $\mathbf{u} = (u, v)^T$ is written $\mathbf{u} = \mathbf{U} + \mathbf{u}'$ where $\mathbf{u}' = (u', v')^T$ is the deviation
 251 to the average velocity. Then we define the tensor

$$\Phi = \frac{1}{h^3} \int_0^h \mathbf{u}' \otimes \mathbf{u}' dz \quad (2.43)$$

252 which will be called thereafter enstrophy because it is homogeneous to the square of a
 253 vorticity. The components of this two-dimensional symmetrical and anisotropic tensor
 254 are defined by $\Phi = \varphi_{11} \mathbf{e}_x \otimes \mathbf{e}_x + \varphi_{12} \mathbf{e}_x \otimes \mathbf{e}_y + \varphi_{12} \mathbf{e}_y \otimes \mathbf{e}_x + \varphi_{22} \mathbf{e}_y \otimes \mathbf{e}_y$. We can write

$$\langle u^2 \rangle = U^2 + h^2 \varphi_{11}; \quad \langle uv \rangle = UV + h^2 \varphi_{12}; \quad \langle v^2 \rangle = V^2 + h^2 \varphi_{22}. \quad (2.44)$$

255 The enstrophy terms are not negligible because the velocity \mathbf{u} is not constant in the
 256 depth. This implies that $\langle \mathbf{u} \otimes \mathbf{u} \rangle \neq \mathbf{U} \otimes \mathbf{U}$. On the contrary, at order 0, as it is shown
 257 above, the variations of the velocity with the depth is linear as in a planar Couette flow.
 258 Furthermore, at order 1, the velocity profile can be different from a linear profile. With the
 259 enstrophy tensor, the nonlinear term is written $\langle \mathbf{u} \otimes \mathbf{u} \rangle = \mathbf{U} \otimes \mathbf{U} + h^2 \Phi$. The introduction
 260 of the enstrophy as an additional variable of the model guarantees a well-posed model
 261 i.e. with an energy conservation equation (see the discussion of the two-equation model
 262 (2.49) below), in the case of a non-constant velocity profile.

263 In tensor form, the depth-averaged momentum equation can be written

$$\frac{\partial h\mathbf{U}}{\partial t} + \mathbf{div}(h\mathbf{U} \otimes \mathbf{U} + h^3\boldsymbol{\Phi}) = \frac{3}{\varepsilon Re} \left(\frac{\boldsymbol{\tau}_e}{2} - \frac{\mathbf{U}}{h} \right) + \kappa h \mathbf{grad} K + O(\varepsilon). \quad (2.45)$$

264 *2.4.3 Enstrophy equation*

265 The derivation of the conservative part of the equations for the tensors $h^3\boldsymbol{\Phi}$ and $h^2\boldsymbol{\Phi}$
 266 can be found in [Teshukov (2007)] and for the tensor $\boldsymbol{\Phi}$ in [Richard et al. (2019a)], in both
 267 cases under the approximation of a weakly sheared flow, which means that the tensor
 268 $\langle \mathbf{u}' \otimes \mathbf{u}' \otimes \mathbf{u}' \rangle$ is negligible. In the present case, the third-order tensor $\langle \mathbf{u}' \otimes \mathbf{u}' \otimes \mathbf{u}' \rangle$ can
 269 be consistently evaluated at order 0. At this order, the flow is a plane Couette flow with
 270 a linear velocity profile, which implies that this third-order tensor is equal to zero at
 271 order zero. The structure of the conservative part of the equations of Teshukov can thus
 272 be found consistently even if this flow is not weakly sheared.

The enstrophy tensor is expanded as $\boldsymbol{\Phi} = \boldsymbol{\Phi}^{(0)} + \varepsilon\boldsymbol{\Phi}^{(1)} + O(\varepsilon^2)$ with at order 0,

$$\boldsymbol{\Phi}^{(0)} = \frac{1}{12} \boldsymbol{\tau}_e \otimes \boldsymbol{\tau}_e$$

273 and at order 1,

$$\boldsymbol{\Phi}^{(1)} = \kappa Re \frac{h}{24} (\boldsymbol{\tau}_e \otimes \mathbf{grad} K + \mathbf{grad} K \otimes \boldsymbol{\tau}_e) \quad (2.46)$$

274 It follows that

$$\boldsymbol{\Phi} - \frac{\mathbf{U} \otimes \mathbf{U}}{3h^2} + \frac{1}{12h^2} \left(\mathbf{U} \otimes \mathbf{U} - \frac{h^2 \boldsymbol{\tau}_e \otimes \boldsymbol{\tau}_e}{4} \right) = O(\varepsilon^2). \quad (2.47)$$

The enstrophy equation can be consistently written at first order as

$$\begin{aligned} \frac{\partial h\boldsymbol{\Phi}}{\partial t} + \mathbf{div}(h\boldsymbol{\Phi} \otimes \mathbf{U}) - 2h(\mathbf{div} \mathbf{U}) \boldsymbol{\Phi} + \mathbf{grad} \mathbf{U} \cdot h\boldsymbol{\Phi} + h\boldsymbol{\Phi} \cdot (\mathbf{grad} \mathbf{U})^T \\ = -\frac{1}{\varepsilon Re} \frac{B}{h} \left[\boldsymbol{\Phi} - \frac{\mathbf{U} \otimes \mathbf{U}}{3h^2} + \frac{1}{12h^2} \left(\mathbf{U} \otimes \mathbf{U} - \frac{h^2 \boldsymbol{\tau}_e \otimes \boldsymbol{\tau}_e}{4} \right) \right] + O(\varepsilon) \end{aligned} \quad (2.48)$$

275 where B is an arbitrary dimensionless constant. Details on this derivation are given in
 276 Appendix A.

Physically, B controls the relaxation of the enstrophy $\boldsymbol{\Phi}$ on the tensor $\mathbf{U} \otimes \mathbf{U}$. Considering a large value of B yields

$$\boldsymbol{\Phi} \approx \frac{1}{4h^2} \mathbf{U} \otimes \mathbf{U} + \frac{1}{48} \boldsymbol{\tau}_e \otimes \boldsymbol{\tau}_e$$

277 and leads back to a two-equation system of equation for h and \mathbf{U} where the averaged
 278 momentum balance reads

$$\frac{\partial h\mathbf{U}}{\partial t} + \mathbf{div} \left(\frac{5}{4} h\mathbf{U} \otimes \mathbf{U} + \frac{h^3}{48} \boldsymbol{\tau}_e \otimes \boldsymbol{\tau}_e \right) = \frac{3}{\varepsilon Re} \left(\frac{\boldsymbol{\tau}_e}{2} - \frac{\mathbf{U}}{h} \right) + \kappa h \mathbf{grad} K. \quad (2.49)$$

279 Unfortunately, this two-equation system does not admit an energy conservation equation
 280 because of the factor 5/4 instead of 1 in the momentum flux (the justification is similar
 281 to the case studied in Richard et al. (2019b)). The only consistent two-equation system
 282 with a factor 1 in the momentum flux in front of $h\mathbf{U} \otimes \mathbf{U}$ has a flux equal to $h\mathbf{U} \otimes \mathbf{U} +$
 283 $(1/12)h^3\boldsymbol{\tau}_e \otimes \boldsymbol{\tau}_e$. Due to the anisotropy of the tensor $\boldsymbol{\tau}_e \otimes \boldsymbol{\tau}_e$, the second term of this flux
 284 does not behave as a pressure as for example the term $gh^2\mathbf{I} \cos \theta/2$ in the usual [nonlinear](#)
 285 [shallow-water](#) equations (\mathbf{I} being the identity tensor). As a result, even this two-equation
 286 system does not admit an energy conservation equation in conservative form.

On the contrary, the three-equation system (2.37), (2.45) and (2.48) does admit an energy conservation equation, which can be written

$$\begin{aligned} \frac{\partial he}{\partial t} + \operatorname{div}(he\mathbf{U} + h^3\boldsymbol{\Phi} \cdot \mathbf{U}) &= \left[\frac{3}{\varepsilon Re} \left(\frac{\boldsymbol{\tau}_e}{2} - \frac{\mathbf{U}}{h} \right) + \kappa h \mathbf{grad} K \right] \cdot \mathbf{U} \\ &\quad - \frac{1}{\varepsilon Re} \frac{Bh}{2} \left(\operatorname{tr} \boldsymbol{\Phi} - \frac{\mathbf{U} \cdot \mathbf{U}}{4h^2} - \frac{\boldsymbol{\tau}_e \cdot \boldsymbol{\tau}_e}{48} \right) + O(\varepsilon) \end{aligned} \quad (2.50)$$

where the energy e is $e = \mathbf{U} \cdot \mathbf{U}/2 + h^2 \operatorname{tr} \boldsymbol{\Phi}/2$. Because of the existence of this energy conservation equation in conservative form, the three-equation system is clearly preferable to all consistent two-equation systems.

2.5 Inertialess limit

Before completing our flow description with a model for partial wetting conditions, let us underline the link between the shallow-water three-equation model (2.37), (2.45) and (2.48), which we have derived so far, and the surface equations that are usually employed based on lubrication theory. A more complete justification of the link between shallow-water equations and lubrication ones can be found in Bresch & Noble (2007).

In the limit of a vanishing Reynolds number, the momentum balance (2.45) reduces to

$$\mathbf{U} = \frac{h}{2} \boldsymbol{\tau}_e + \varepsilon^3 Ca \frac{h^2}{3} \mathbf{grad} K \quad (2.51)$$

where $Ca = \frac{\gamma}{\mu u_0}$ is a capillary number. Following the usual approximation of the lubrication theory, the curvature K of the free surface can be approached by Δh . As a consequence, the mass balance (2.37) yields (Oron *et al.* 1997)

$$\partial_t h + \operatorname{div} \left(\frac{h^2}{2} \boldsymbol{\tau}_e + \varepsilon^3 Ca \frac{h^3}{3} \mathbf{grad} \Delta h \right) = 0, \quad (2.52)$$

which corresponds to the surface equation used by Espín & Kumar (2017) in the appropriate limit (absence of gravity, absorption and disjoining pressure).

Interestingly, shallow-water systems of equations, equivalent to lubrication equations of the form (2.52) in the limit of a vanishing Reynolds number, have been used to prove global existence of nonnegative weak solutions of lubrication equations (Bresch *et al.* 2019).

2.6 Disjoining pressure

In order to account for dewetting phenomena and the displacement of contact lines, we introduce a regularization of the jump of surface energy from the liquid-gas interface ($\gamma_{lg} = \gamma$) to the solid-gas interface ($\gamma_{sg} = \gamma \cos(\theta_s) < \gamma_{sl}$) by means of a disjoining energy $e_d(h)$ function of the free surface elevation. For convenience as will be discussed later in section 2.7, we set the reference of the dimensionless surface energy to zero at a flat solid-gas interface, so that the dimensionless surface energy at the wall is equal to $\kappa(\cos(\theta_s) - 1)$.

We adopt the classical formulation proposed by Derjarguin (Churaev & Sobolev 1995), where the disjoining energy density reads

$$e_d(h) = \frac{(n-1)(m-1)}{n-m} \kappa [\cos(\theta_s) - 1] \left[\frac{1}{1-n} \left(\frac{h^*}{h} \right)^{n-1} - \frac{1}{1-m} \left(\frac{h^*}{h} \right)^{m-1} \right], \quad (2.53)$$

where $n > m$, and varies accordingly from 0 in the bulk of the liquid ($h \gg h^*$) to

317 $\kappa[\cos(\theta_s) - 1]$ at the precursor film thickness h^* . The precursor film $h = h^*$ thus plays
 318 the role of the solid-gas interface. The introduction of a precursor film is an elegant way to
 319 deal with the singularity of the viscous stress at the contact line. Another approach is the
 320 introduction of a slip at the wall. Comparisons of the slip and precursor-film approaches
 321 show that they are more or less equivalent (Sibley *et al.* 2015). Yet Diez & Bertozzi
 322 (2000) found the former less numerically demanding.

323 Associated to the disjoining energy is a disjoining pressure

$$\Pi(h) = -\frac{de_d}{dh} = \frac{(n-1)(m-1)}{n-m} \frac{\kappa[1 - \cos(\theta_s)]}{h^*} \left[\left(\frac{h^*}{h}\right)^n - \left(\frac{h^*}{h}\right)^m \right] \quad (2.54)$$

324 so that the pressure in the liquid reads $p = -K - \Pi(h)$.

325 The disjoining pressure is negative for $h > h^*$ and positive for $h < h^*$ which guaranties
 326 the stability of the precursor film. At a contact line, the disjoining pressure promotes a
 327 gradient of pressure which drives the liquid out of the precursor film.

328 In line with the observations of Diez & Bertozzi (2000), we observe that the Frumkin-
 329 Derjaguin disjoining energy (2.53) enables to take quite large values h^* of the precursor
 330 film while modelling correctly the apparent static contact angle. Besides, the precursor-
 331 film model acts as a low-pass filter : drops with a height which is less than $2h^*$ are
 332 absorbed by the precursor film. As a consequence, with this model, the minimal size of
 333 the droplets that are represented is controlled by h^* .

334

2.7 Augmented Formulation

335 In order to mimic the dynamics of shear driven sliding droplets, a mathematical frame-
 336 work has been developed. The derived formulation needs to overcome the limitations of
 337 previous attempts, especially the correct inclusion of surface tension, which is required in
 338 order to capture correctly the shape of the droplets. A second requirement is to obtain a
 339 conservative hyperbolic formulation and to guarantee the consistency with the long-wave
 340 expansion in the appropriate limit. These properties would enable to develop efficient
 341 numerical schemes which preserve the energy of the flow.

342 Lastly, partial wetting has to be accounted for and must enable to capture the hysteresis
 343 of the static contact angle. This last requirement will allow for a correct description of
 344 droplets shedding and water accumulation. Bresch *et al.* (2020) developed an augmented
 345 formulation for surface tension, accounting for the full curvature of the free surface, thus
 346 improving over the initial formulation of Noble & Vila (2014) and Bresch *et al.* (2016)
 347 which was limited to linearised curvature of the free surface in the long wave limit.

348 In short, the idea is to introduce an additional variable with the dimension of a
 349 velocity whose kinetic energy is equal to the surface energy of the film. By writing
 350 a transport equation for this additional variable, we are able to recast shallow-water
 351 equations with full surface tension terms into an ‘‘augmented’’ system of equations with
 352 a skew-symmetric structure with respect to the L^2 scalar product which makes the proof
 353 of energy estimates. Additionally, the design of compatible numerical scheme is made
 354 easier as surface tension terms are then recast as generalized diffusion terms.

355 Following Bresch *et al.* (2020), we introduce a vector variable \mathbf{W} which is co-linear to
 356 the gradient of the free-surface location, $\mathbf{p} = \mathbf{grad}h$ and verifies

$$\mathbf{W} = \frac{\sqrt{\kappa}}{\sqrt{h}} \alpha(q^2) \mathbf{p}, \quad (2.55a)$$

$$\text{with } \alpha(q^2) = \frac{\sqrt{2}}{q} (\sqrt{1+q^2} - 1)^{1/2} = \sqrt{2} (\sqrt{1+q^2} + 1)^{-1/2}, \quad (2.55b)$$

$$q = \|\mathbf{grad}h\| = \|\mathbf{p}\|. \quad (2.55c)$$

357 Note that, in this context, \mathbf{W} has the dimension of a velocity and transforms the capillary
358 energy density into a virtual kinetic energy as

$$\frac{1}{2}h \|\mathbf{W}\|^2 = \kappa(\sqrt{1+q^2} - 1). \quad (2.56)$$

359 Again, in order to make reversible the relation between the additional velocity \mathbf{W} and
360 the gradient $\mathbf{grad} h$, the constant $\kappa = \gamma/\rho$ has been subtracted to the usual definition of
361 the surface capillary energy, which does not affect the dynamics of the flow.

362 The system of dimensionless equations (2.37), (2.45) and (2.48) is then modified into

$$\frac{\partial h}{\partial t} + \mathbf{div}(h\mathbf{U}) = 0, \quad (2.57a)$$

$$\begin{aligned} \frac{\partial h\mathbf{U}}{\partial t} + \mathbf{div}(h\mathbf{U} \otimes \mathbf{U} + h^3\boldsymbol{\Phi}) &= \frac{3}{Re} \left(\frac{\boldsymbol{\tau}_e}{2} - \frac{\mathbf{U}}{h} \right) + h \mathbf{grad} \Pi(h) \\ &+ \mathbf{div} \left[h (\mathbf{grad}(\mathbf{f}_1 \cdot \mathbf{W}))^T \right] - \mathbf{grad}(\mathbf{f}_2 \cdot \mathbf{W}), \end{aligned} \quad (2.57b)$$

363

$$\frac{\partial h\mathbf{W}}{\partial t} + \mathbf{div}(h\mathbf{W} \otimes \mathbf{U}) = -\mathbf{f}_1 \cdot \mathbf{div} \left[h (\mathbf{grad} \mathbf{U})^T \right] - \mathbf{f}_2 \mathbf{div} \mathbf{U}, \quad (2.57c)$$

$$\begin{aligned} \frac{\partial h\boldsymbol{\Phi}}{\partial t} + \mathbf{div}(h\boldsymbol{\Phi} \otimes \mathbf{U}) - 2h(\mathbf{div} \mathbf{U})\boldsymbol{\Phi} + \mathbf{grad} \mathbf{U} \cdot h\boldsymbol{\Phi} + h\boldsymbol{\Phi} \cdot (\mathbf{grad} \mathbf{U})^T \\ = -\frac{1}{Re} \frac{B}{h} \left[\boldsymbol{\Phi} - \frac{\mathbf{U} \otimes \mathbf{U}}{3h^2} + \frac{1}{12h^2} \left(\mathbf{U} \otimes \mathbf{U} - \frac{h^2}{4} \boldsymbol{\tau}_e \otimes \boldsymbol{\tau}_e \right) \right], \end{aligned} \quad (2.57d)$$

364 where the second-order tensor \mathbf{f}_1 is given by

$$\mathbf{f}_1(h, \mathbf{W}) = \sqrt{\kappa} \sqrt{h} \left(1 + \frac{h}{4\kappa} \|\mathbf{W}\|^2 \right)^{-1/2} \left(\mathbf{I} - \frac{h}{4\kappa} \left(1 + \frac{h}{2\kappa} \|\mathbf{W}\|^2 \right)^{-1} \mathbf{W} \otimes \mathbf{W} \right) \quad (2.57e)$$

365 and the vector \mathbf{f}_2 by

$$\mathbf{f}_2(h, \mathbf{W}) = \frac{h\mathbf{W}}{2} \left(1 + \frac{h}{2\kappa} \|\mathbf{W}\|^2 \right)^{-1}. \quad (2.57f)$$

366

367 An advantage of the above formulation is to commute the third-order capillary term
368 $\mathbf{grad} K$ in the averaged momentum balance into second-order generalized diffusion terms
369 in (2.57b), a simplification that turns out useful in numerical simulations, especially on
370 unstructured meshes. The principal advantage of (2.57) is the skew-symmetry of these
371 second-order terms with respect to the L^2 scalar product and allows for the construction
372 of numerical schemes which conserve the energy (see below).

373 Note that the definitions (2.55a), (2.57e) and (2.57f) of the additional velocity \mathbf{W}
374 and functions \mathbf{f}_1 and \mathbf{f}_2 remain unchanged when the kinematic surface tension γ/ρ is
375 substituted for κ .

376 Dimensional equations are given in Appendix B.

377 3 Simulations

378 An in-house 2D numerical solver implementing the proposed model (2.57) has been
379 developed. The code is written in Julia, and uses the method of line. This method
380 adopts a semi-discrete form of the model: an o.d.e. system is obtained after the spatial

381 discretization is implemented. The spatial discretization of the model uses both the
 382 finite volume method for the hyperbolic terms at the l.h.s. of the equations and the
 383 finite difference method for the remaining terms on the r.h.s. The MUSCL method is
 384 employed along with a slope limiter (optional), ensuring a numerical scheme of second
 385 order in space for the hyperbolic part of the equations. The “minmod”, “superbee” and
 386 “Van-Leer” limiters have been implemented. Their objective is to ensure the connection
 387 between the zones of strong and weak gradients as finite volume schemes of order greater
 388 than one are known to be unstable at strong gradients (Godunov & Bohachevsky 1959).
 389 The choice of limiters enables to switch from a scheme of second order in the regions where
 390 the solution is smooth to a scheme of first order where the gradients are important to
 391 ensure total variation diminishing property of the global scheme. The choice of the limiter
 392 has a strong impact on the numerical diffusion: this diffusion artificially smoothes the
 393 solution, which is to be avoided, but makes the diagram more robust to sudden oscillations
 394 near the discontinuities. In implemented limiters, “minmod” is the most diffusive (and
 395 stable) and “superbee” the most precise (but can generate digital oscillations). “Van-
 396 Leer” is a compromise between these two extremes. The remaining terms are discretized
 397 by centered finite differences of second-order. Integration in time of the obtained system
 398 of o.d.e. requires the selection of a time solver which satisfies the following constraints:

399 (i) The presence of a steep fronts at the contact lines implies a “stiff” problem, which
 400 requires the use of an implicit solver. This means that a large-dimensional linear system
 401 $(N_x \times N_y \times 8)^2$ must be solved.

402 (ii) Solving this linear system requires the computation of the associated Jacobian. Its
 403 finite difference approximation is expensive and imprecise. This requires to make use of
 404 sparse matrices in order to limit its memory storage.

405 In comparison to the scheme developed by Bresch *et al.* (2020), we have avoided a
 406 semi-implicit scheme for the surface tension terms. Instead of using an implicit solver,
 407 we have chosen to use an Explicit Strong Stability-Preserving Runge-Kutta (SSPRK)
 408 method (Gottlieb *et al.* 2001). This method is a Runge-Kutta method that preserves the
 409 stability of first order methods. They have proved helpful in solving hyperbolic partial
 410 differential equations. Being explicit, this method does not require the computation of
 411 the Jacobian, neither the solution of a linear system. This leads to a significant reduction
 412 of the computational time as well as easy-to-write parallelization of the code. A CUDA
 413 compatible version of the code has been developed, which allows to perform simulations
 414 on a GPU. The SSPRK method enables to control the time step according to a local
 415 truncation error, which can be used to control the accuracy of the solution. The time step
 416 is controlled by a Proportional-Integral algorithm that adjusts the time step according
 417 to the local truncation error. Absolute local threshold is set to 10^{-6} and relative local
 418 threshold is set to 10^{-3} .

419 A reprojection routine is used to ensure that the augmented variable \mathbf{W} stay close to
 420 its definition (see (2.55a)): this is mandatory when the variable become discontinuous,
 421 which will be the case near the triple point. The reprojection is done at each timestep.

422 Simulations have been carried out on an AMD Ryzen 9 3950X 16-Core Processor and a
 423 GeForce RTX 3080 Ti (10'240 CUDA Core). The performance of the numerical code has
 424 been evaluated for a benchmark consisting of the simulation of a two-dimensional droplet
 425 for the flow conditions corresponding to figure 10 with no hysteresis and $N \times 3N = 2 \times 10^6$
 426 nodes, aborting the simulations at time $t = 20$. Single-thread, mutli-thread and GPU
 427 runs have been compared. A single-thread run lasts 8018 seconds, an execution time,
 428 which is lowered to 2771 for 4 threads, but only reduces to 2001 seconds for 8 threads
 429 and actually increase to 2050 seconds for 16 threads. In contrast, the GPU simulation
 430 lasted only 189 seconds. Tests of convergence show a quadratic dependence of the time

431 step δt on the mesh size Δ in the form $\delta t = O(\Delta^2)$ as expected from the second-order
 432 generalized-diffusion nature of the capillary terms.

433 3.1 Contact angle hysteresis

434 The adherence of the sessile drops is the hallmark of static contact angle hysteresis.
 435 Small drops have the ability to deform and resist the onset of motion due to the shear of
 436 the gas flow since a pressure gradient may be sustained between the front and the rear
 437 of the drop as a result of the difference between the contact angle at its front and back.

438 Numerical implementation of contact angle hysteresis is generally based on an evalu-
 439 ation of the triple line orientation with respect to the orientation of the flow (Ding &
 440 Spelt 2008). For instance, using a precursor film formulation and a Frumkin-Derjaguin
 441 disjoining pressure, Ahmed *et al.* (2014) tracked the location of the contact line point at
 442 which the contact line was orthogonal to the flow direction, thus defining the back and
 443 front of the drop. However, Ahmed *et al.* computed only one drop at a time and this
 444 approach seems difficult to apply for several drops when coalescence or splitting may
 445 occur.

446 As a first approach, the orientation of the contact line with respect to the flow has been
 447 evaluated by computing $\mathbf{U} \cdot \mathbf{grad} h$. The front of the drop is identified as $\mathbf{U} \cdot \mathbf{grad} h <$
 448 0 and the static contact angle θ_s is then set to its advancing value θ_a . Conversely, if
 449 $\mathbf{U} \cdot \mathbf{grad} h > 0$, θ_s is adjusted to the receding contact angle θ_r . However, this method
 450 leads to numerical difficulties. The first one is the sharp jump of surface energies at the
 451 edges of the drop, i.e. for $\mathbf{U} \perp \mathbf{grad} h$. Small fluctuations of the orientation of the contact
 452 line at these edges thus promote sharp surface forces, which generate oscillations of the
 453 contact line. These numerical spurious waves propagate, grow, and may lead to failures
 454 of the numerical simulations.

455 In order to avoid this problem, the front and back of the moving drops are identified
 456 based on $\text{div}(h\mathbf{U}) = -\partial h/\partial t$. Thus, the front of the drop is identified if mass is gained,
 457 i.e. $\text{div}(h\mathbf{U}) < 0$. The limit of the front and back regions of the drop does not depend
 458 on the orientation of the contact line with this definition. A direct consequence is that
 459 the local contact angle may not switch sharply from θ_a to θ_r by changing the orientation
 460 of the contact line. This proves to be sufficient to eliminate the occurrence of spurious
 461 oscillations at the contact line.

462 In practice, the discontinuity of the value of the static contact angle has been regular-
 463 ized with a hyperbolic tangent.

$$\theta_s = \frac{\theta_a + \theta_r}{2} + \frac{\theta_r - \theta_a}{2} \tanh \left[\frac{\text{div}(h\mathbf{U})}{\varepsilon'} \right] \quad (3.1)$$

464 where ε' has been taken sufficiently low.

465 3.2 Simulations of single drops

466 Simulations of the dynamics of sessile drops under the action of a shear stress have
 467 been conducted initially without taking into account the hysteresis of the contact angle.

468 Convergence of our numerical scheme with respect to the grid mesh has been checked
 469 by conducting simulations in one dimension (i.e. assuming all derivatives $\partial_y = 0$ with
 470 only one cell in the y direction) with periodic boundary conditions. A spherical cap drop
 471 is placed at initial time in the numerical domain. The characteristic height of the drop
 472 is $h_0 = 0.1$ mm. Physical properties correspond to water ($\mu = 10^{-3}$ Pa.s, $\rho = 10^3$ kg/m³
 473 and $\gamma = 75$ mN/m) and the wall shear stress τ_e is adjusted to $\tau_e = 8$ Pa.s. The Reynolds
 474 and Weber numbers are thus $Re = 80$ and $We = 0.85$. These values are unchanged
 475 throughout this section.

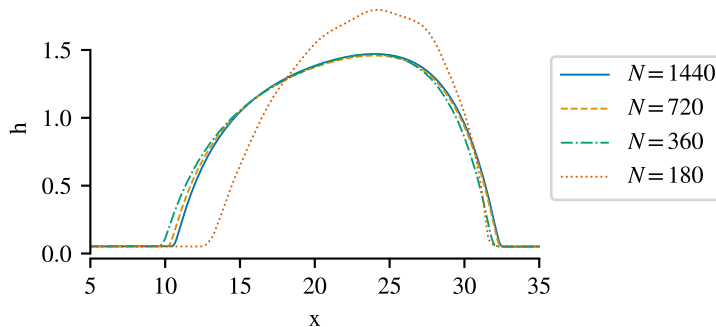


Figure 2: Convergence test in 1D. $L = 7.2$ mm, contact angle $\theta_s = 30^\circ$
 $\Delta/h^* = 2$ for $N = 720$.

476 The numerical domain extension is 7.2 mm. The precursor film thickness is set to
 477 $h^* = 0.05$, which corresponds to $5 \mu\text{m}$. Figure 2 presents the result of our convergence
 478 test with respect to the mesh size Δ , or number of mesh nodes N . The final shape of
 479 the droplet is reported at the end of the simulation when a constant shape and speed are
 480 achieved. However, low values of N are associated to spurious oscillations of the drop. A
 481 number $N = 720$ of nodes is sufficient to approach satisfactorily the shape of the sliding
 482 drop, as simulations with $N = 720$ and $N = 1440$ provides close final shapes of the
 483 drop. Numerical tests with different precursor film thicknesses (not shown) indicate that
 484 the mesh size Δ must be of the order of h^* in order to prevent the onset of spurious
 485 oscillations which emanate from an inadequate representation of the contact line region
 486 of the drop. We thus conclude that a ratio $\Delta/h^* = 2$ is sufficient to capture the transition
 487 region which replaces a sharp contact line within the disjoining pressure description of
 488 partial wetting. A value of $\Delta/h^* = 2$ has thus been used hereinafter for every simulations
 489 presented in this work. However, a lower resolution, i.e. $\Delta/h^* = 4$ is still acceptable.

490 Figure 3 presents the distribution of the velocity U and enstrophy φ within the droplet
 491 at final time. The velocity U is almost constant in the bulk of the droplet and varies only
 492 at the front and back of the drop as the film thickness reduces to precursor film thickness.
 493 Indeed, for travelling-wave solutions, i.e. solutions whose shape and speed do not vary
 494 with time, the mass balance (2.37) can be rewritten in the moving frame $\xi = x - u_{\text{drop}}t$
 495 and integrated to yield

$$h(U - u_{\text{drop}}) = h^* \left(\frac{\tau_e h^*}{2} - u_{\text{drop}} \right) \quad (3.2)$$

496 where the constant flow rate in the moving frame of reference is expressed at the r.h.s.
 497 of (3.2) from the Nusselt solution $h = h^*$. Therefore $h^* \ll 1$ implies that $U \approx u_{\text{drop}}$
 498 whenever $h \gg h^*$.

499 Instead of plotting φ , we choose to show $h^2\varphi$ which corresponds to the contribution
 500 of the deviations of the velocity profile $u - U$ to the kinetic energy. We compare $h^2\varphi$ to
 501 U^2 by computing the shape factor

$$\alpha = \frac{\langle u^2 \rangle}{\langle u \rangle^2} = 1 + \frac{h^2\varphi}{U^2} \quad (3.3)$$

502 The shape factor α does not deviate much from the value $4/3$ corresponding to the
 503 Couette flow solution (2.28). As a consequence, φ adopts large values at the edges of the

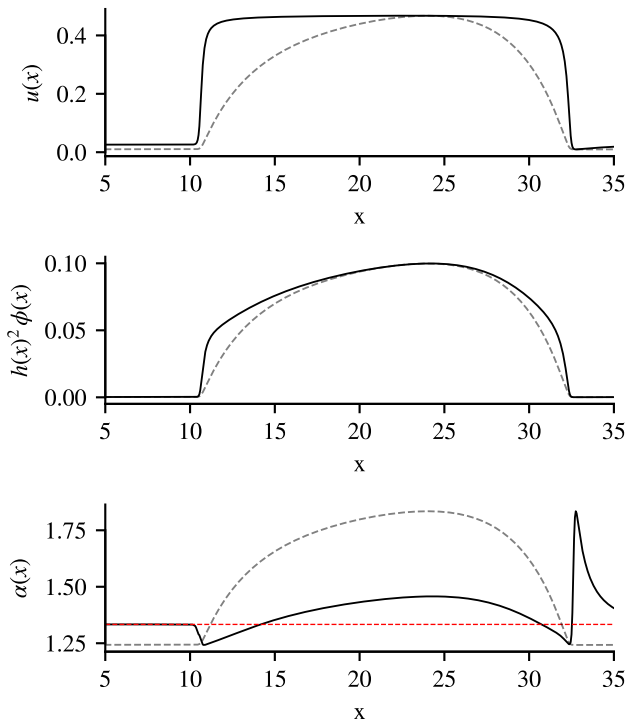


Figure 3: Distribution of averaged velocity U , entrophy weighted by the square of the thickness, $h^2\varphi$ and shape factor $\alpha = 1 + h^2\varphi/U^2$ (the red horizontal line shows the value $\alpha = 4/3$) for the 1D droplet of figure 2 ($N = 1440$, $h^* = 0.05$). The dashed black curves show the depth profile of the droplet.

504 droplet, so that displaying φ instead of $h^2\varphi$ gives the false impression that the entrophy
 505 is negligible in the bulk of the droplet. A value of the shape factor equal to $4/3$ indicates
 506 a linear velocity profile in the depth. A shape factor smaller than $4/3$ indicates a convex
 507 velocity profile i.e. with a larger shear near the bottom than close to the free surface,
 508 while the opposite is true for a shape factor larger than $4/3$, which denotes a concave
 509 profile, with a stronger shear near the free surface than near the bottom. The distribution
 510 of the shape factor shows that there is a strong shear effect close to the free surface in
 511 the center of the droplet, resulting in a shape factor larger than $4/3$. At the edges of the
 512 droplet, the curvature of the velocity profile has the opposite sign.

513 Figure 4 illustrates the influence of the precursor film thickness on the shape of one-
 514 dimensional drops which have reached a steady state. For a large value of h^* , the
 515 extension of the drop length is larger, and the front is more rounded. The front shape
 516 of the drop is more impacted than its back shape by the precursor film thickness. The
 517 maximum elevation of the drop also decreases as h^* is raised.

518 Figure 5 discusses the influence of the precursor film thickness h^* on the drop velocity
 519 u_{drop} and its extension length L . Both of them decrease monotonically with the precursor
 520 film thickness. In agreement with Schwartz & Eley (1998); Sellier *et al.* (2015), we
 521 observe that $1/u_{\text{drop}}$ varies linearly with the logarithm of h^* as expected from (C6)
 522 as a consequence of the dependency of the wall shear dissipative work with respect to h^*
 523 (see Appendix C).

524 We next turn to the simulation of two-dimensional drops. The precursor film thickness

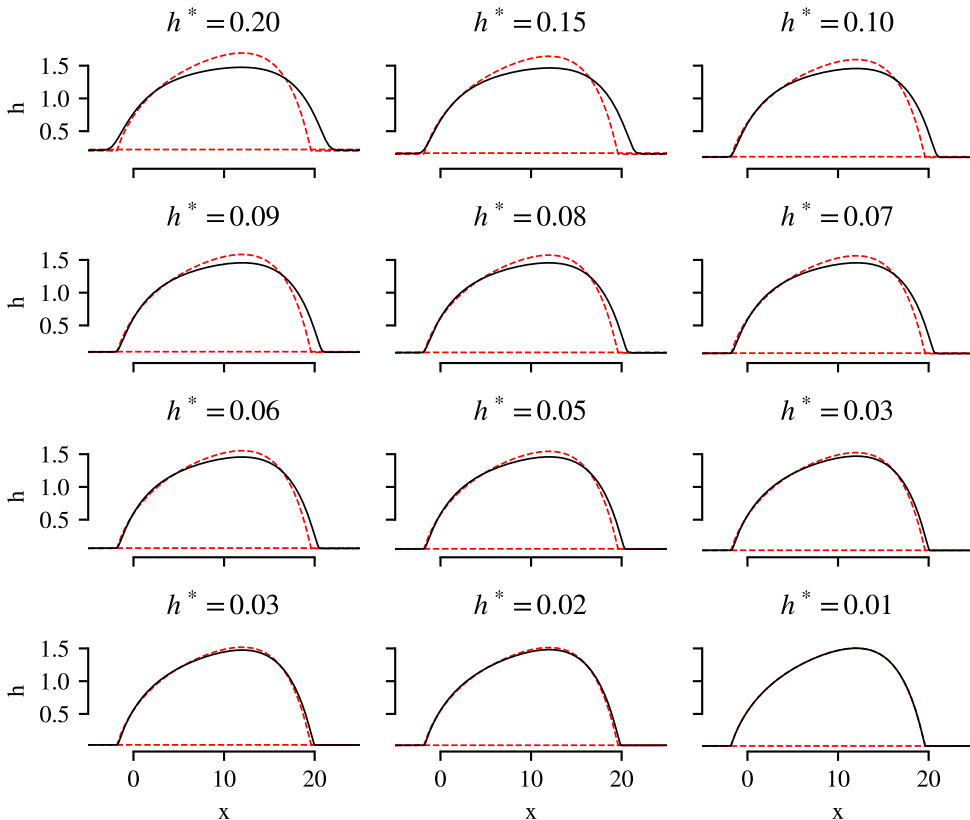


Figure 4: Convergence test in 1D. $L = 7.2$ mm, contact angle $\theta_s = 30^\circ$ and $\Delta/h^* = 2$. Comparison of the drop shapes for different precursor film thicknesses h^* . All simulations have reached steady states. The drop profiles have been aligned to allow for an easy comparison. The red dashed line is the shape of the drop for $h^* = 0.01$.

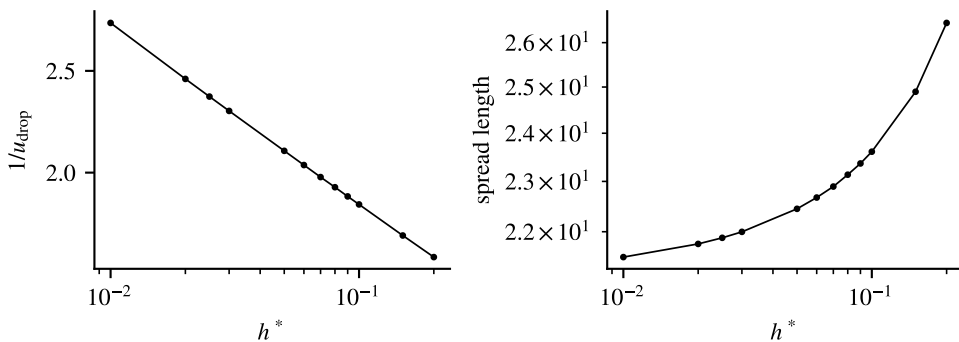


Figure 5: Convergence test in 1D. $L = 7.2$ mm, contact angle $\theta_s = 30^\circ$ and $\Delta/h^* = 2$. Left panel : inverse of drop velocity u_{drop} as a function of the precursor film thickness h^* . Right panel : spread length versus h^* .

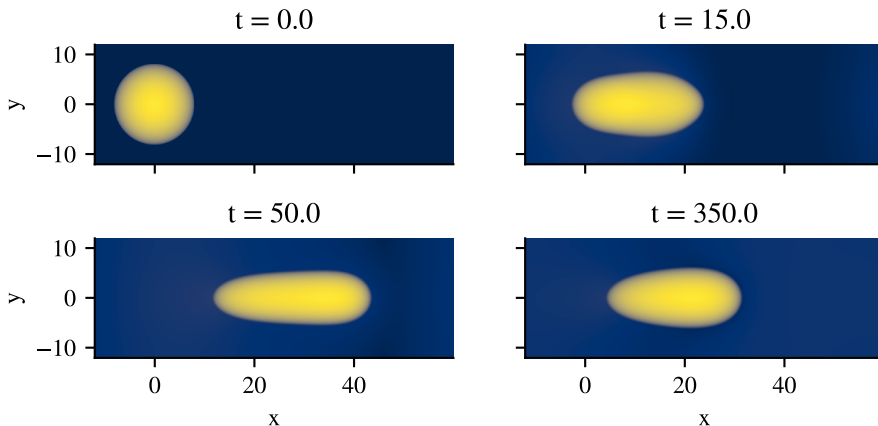


Figure 6: Snapshots of the free surface elevation at different times in a domain of size $7.2 \text{ mm} \times 2.4 \text{ mm}$ with $3N \times N \approx 2 \cdot 10^6$ nodes for a contact angle $\theta_s = 30^\circ$.

525 is set to $h^* = 0.05$, a reasonable trade-off between accuracy and numerical cost as the
 526 mesh size Δ must be chosen of the order of h^* . Two-dimensional simulations have been
 527 performed in a rectangular domain with periodic boundary conditions. At initial time, a
 528 single drop is placed in the numerical domain. Figure 6 illustrates the evolution of the
 529 drop as time is increased. The drop has initially a spherical cap shape, corresponding to
 530 the equilibrium solution in the absence of a shear, with an apparent radius $R_\theta = 0.8 \text{ mm}$.
 531 A constant static contact angle $\theta_s = 30^\circ$ is again imposed.

532 The numerical domain is $7.2 \text{ mm} \times 2.4 \text{ mm}$, or 72 by 24 units. The mesh size to precursor
 533 film thickness is fixed to $\Delta/h^* = 2$ so that the numerical domain is discretized with
 534 $N = 2160$ nodes in the x direction and 720 nodes in the y direction. Mesh cells are
 535 thus squares of dimension $10 \mu\text{m}$. The sessile drop is initially elongated by the shear,
 536 accelerates and, after some oscillations, achieves a constant shape and speed as can be
 537 observed from figure 6. The final shape of the drop is reminiscent of the teardrop shape
 538 of sessile drops entrained by gravity at moderate inclination angles (Ahmed *et al.* 2014).

539 Figure 7 presents the components of the velocity field \mathbf{U} as well as $h^2\Phi$. The velocity
 540 field is nearly constant everywhere and equal to the velocity of the droplet, except
 541 in the vicinity of the contact line. Similarly $h^2\varphi_{12}$ and $h^2\varphi_{22}$ are much smaller than
 542 the component $h^2\varphi_{11}$. As for the 1D droplets discussed in the previous section, the
 543 contribution of the enstrophy to kinetic energy $h^2\text{tr}\Phi/2$ is significant throughout the
 544 droplet.

545 3.3 Hysteresis effect on the drop shape

546 We next turn to the simulations of single sliding drops in the presence of a hysteresis
 547 of the static contact angle. We replicate the simulation presented in figure 6 with a
 548 hysteresis range $2\delta_s = 10^\circ$ so that the advancing and receding contact angles are $\theta_a = 35^\circ$
 549 and $\theta_r = 25^\circ$. We again observe a strong initial elongation of the drop as it starts moving
 550 under the action of the gas shear stress, followed by oscillations leading finally to a
 551 drop propagating with a constant shape and speed (see figure 8). In contrast to the
 552 no hysteresis case, we observe a very different shape of the drop at the final stage of
 553 the simulation, which we may label as inverted-teardrop shape or bullet shape, with
 554 a rounded back and an ogival front. Similar observations have been made by Ding &

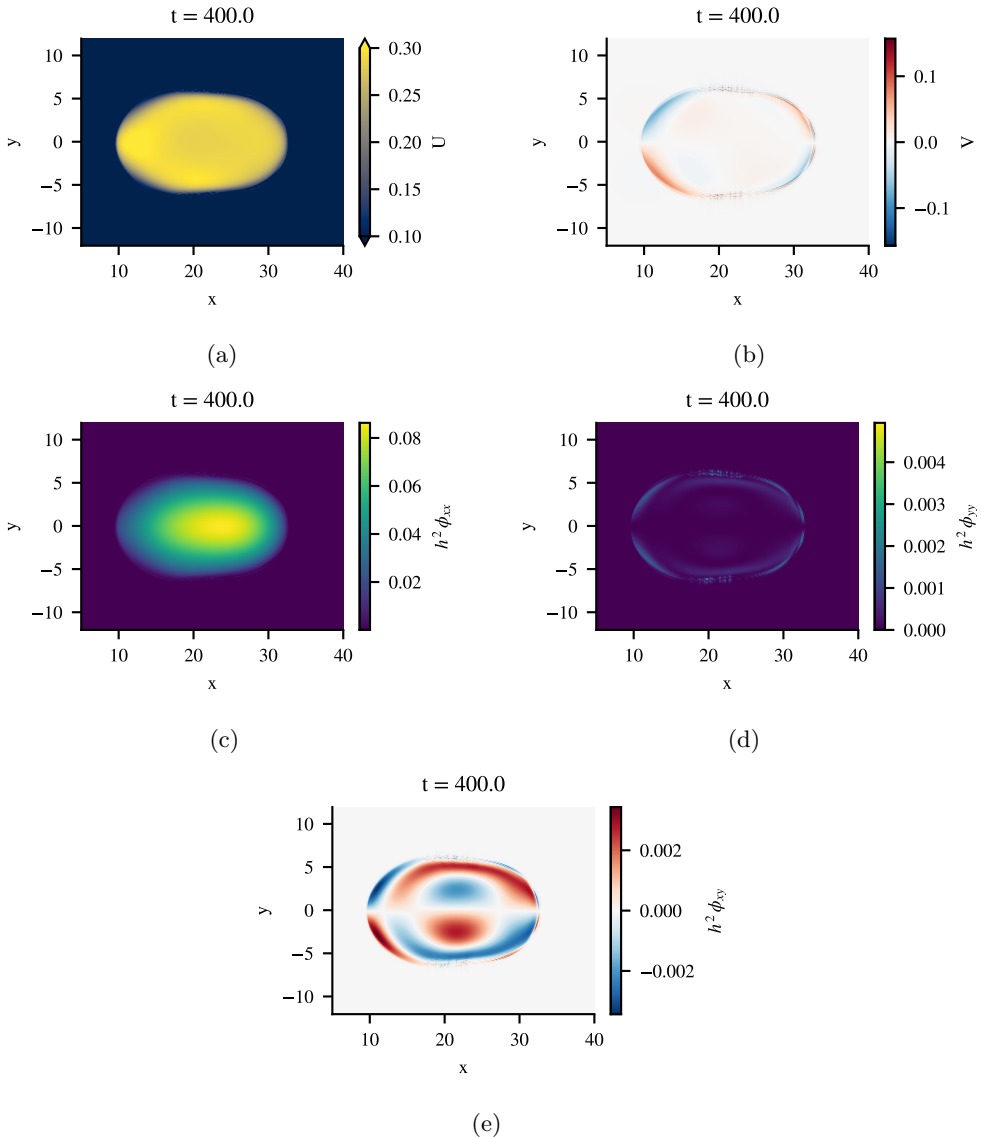


Figure 7: Velocity components, U and V , and enstrophy components $h^2\varphi_{11}$, $h^2\varphi_{22}$ and $h^2\varphi_{12}$ for the droplet in steady state presented in figure 8.

555 Spelt (2008) in their simulations of the onset of motion of shear-driven droplets with
 556 contact-angle hysteresis.

557 As discussed in § 3.1, the simulation of sliding drops in presence of a hysteresis has
 558 been conducted considering the dependence of the static contact angle on $\text{div } h\mathbf{U}$ given
 559 by (3.1) with a regularization parameter $\varepsilon = 10^{-3}$. We checked that the front and
 560 rear of the drop at the end of the simulation were identified similarly by spotting the
 561 accumulation of mass in time (sign of $\text{div } h\mathbf{U}$) or spotting the orientation of the slope
 562 of the free surface (sign of $\mathbf{U} \cdot \mathbf{grad } h$). Figure 9 presents the drop elevation h , and the
 563 distributions of $\mathbf{U} \cdot \mathbf{grad } h$ and $\text{div } h\mathbf{U}$ within the drop, demonstrating that the locations
 564 of the contact line at which mass is accumulated ($\text{div } h\mathbf{U} < 0$) coincides with the front

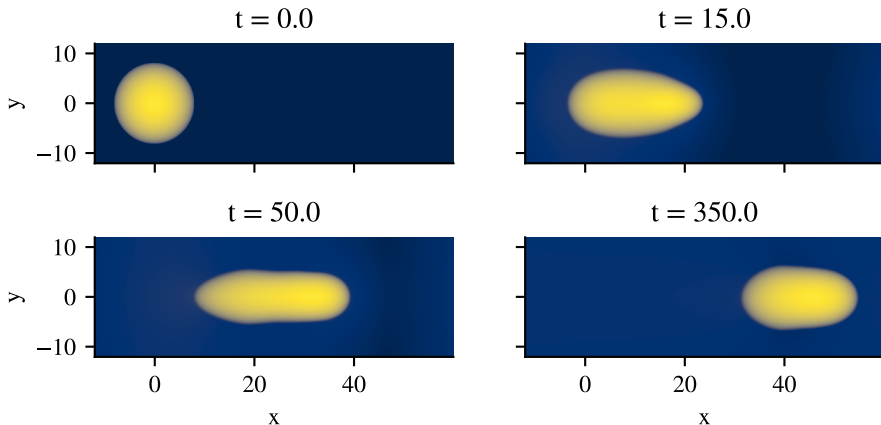


Figure 8: Snapshots of the free surface elevation at different times in a domain of size $7.2 \text{ mm} \times 2.4 \text{ mm}$ with $3N \times N \approx 2 \cdot 10^6$ nodes for a hysteresis $2\delta\theta_s = 10^\circ$ ($\theta_r = 25^\circ$ and $\theta_a = 35^\circ$).

	L	l	S
$2\delta\theta_s$			
0	27.2	12.1	261.64
10	23.5	12.9	245.44
18	19.5	15.5	238.34

Table 1: Drop shape parameters for different hysteresis of the static contact angle $2\delta\theta_s = 0^\circ, 10^\circ$ and 18° .

565 of the drop ($\mathbf{U} \cdot \mathbf{grad} h < 0$). In particular, the region at which, the static contact angle
 566 varies continuously from θ_r to θ_a is restricted to the side edges of the drop (see panel b
 567 of figure 9).

568 As the hysteresis of the static contact angle is increased, the sliding drop continues to
 569 modify its shape, the widest section of the drop moving further to its back. The front
 570 adopts a more and more ogival shape. The width and maximum elevation of the drop
 571 increase, whereas its length diminishes (see figure 10). The variation of the drop length
 572 L , width l and wetting area S is reported table 1.

573 3.4 Dynamics of coarsening

574 We next investigate the coarsening dynamics of a cloud of small droplets deposited at
 575 initial stage on a planar substrate. The parameter set is again chosen to correspond to
 576 water droplets, $\mu = 10^{-3} \text{ Pa}\cdot\text{s}$, $\rho = 1000 \text{ kg/m}^3$, $\gamma = 75 \text{ mN/m}$, undergoing a constant
 577 shear stress $\tau_e = 8 \text{ Pa}$. The numerical domain has a size of $8 \text{ mm} \times 24 \text{ mm}$. The initial
 578 condition consists in a set of 1000 droplets for a total mass 0.22 mm^3 , so that the mean
 579 apparent radius of a sessile droplet is $80 \mu\text{m}$. The mesh size is $\Delta = 10 \mu\text{m}$ and the
 580 precursor film thickness is again $h^* = 5 \mu\text{m}$. These simulations are costly as the number
 581 of nodes reach $N \times 3N = 2 \cdot 10^6$.

582 Figure 11 illustrates the observed dynamics in the absence of contact angle hysteresis.
 583 After an initial absorption of the droplets into the precursor film, droplets of minimal
 584 thickness roughly equal to $15 \mu\text{m}$, that is $3 \times h^*$ start to emerge. This behaviour results

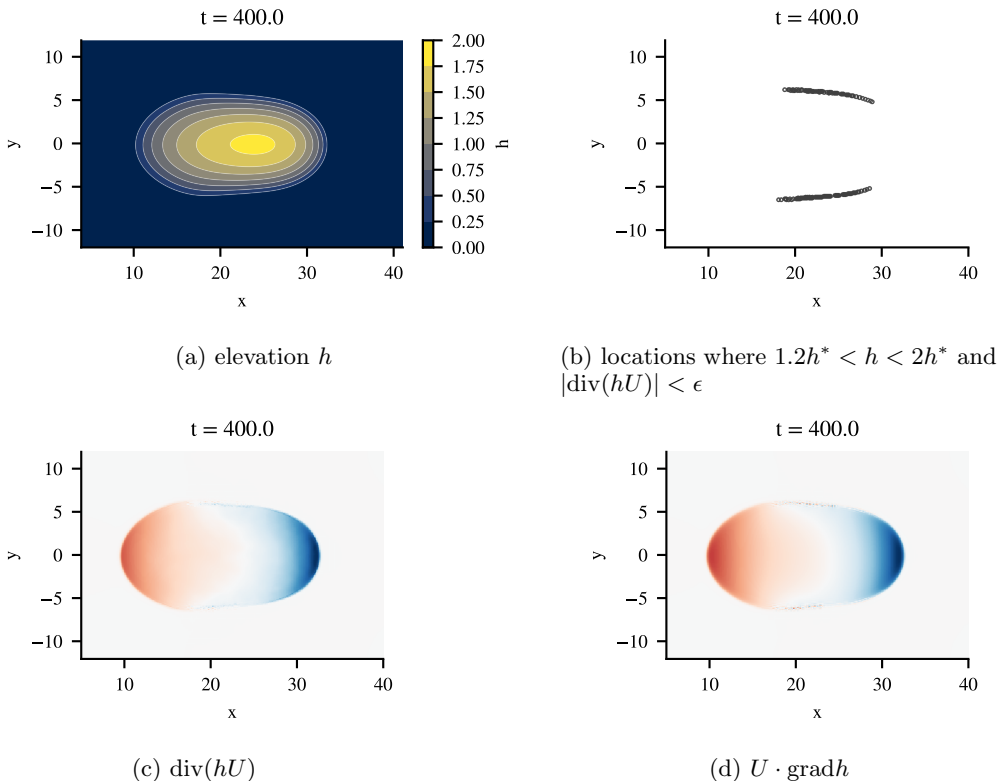


Figure 9: Stationary drop at the end of a simulation for a hysteresis $2\delta\theta_s = 10^\circ$ ($\theta_r = 25^\circ$ and $\theta_a = 35^\circ$)

585 from the disjoining pressure modelling of partial wetting, which acts as a low-pass filter.
 586 The attractive part of the disjoining pressure leads to the absorption of droplets whose
 587 thickness is below two to three times the precursor film thickness h^* . However, the mass
 588 of the film is conserved, and the absorbed droplets raise the mean thickness of the film
 589 above h^* leading to its instability and the formation of larger sliding drops. These drops
 590 have a typical maximal height ranging from 5 to 10 times the thickness h^* of the precursor
 591 film. The later evolution of the film is characterized by the merging of drops as large drops
 592 tend to move faster than smaller ones, catch them and coalesce. As a result, fewer and
 593 fewer drops are observed.

594 In presence of a contact angle hysteresis, a similar evolution of the coarsening dynamics
 595 is observed. However, this scenario seems to be delayed in that case. For instance,
 596 comparing figures 11 and 12, one can notice that the evolution of the merging process
 597 observe without contact angle hysteresis at time $t = 250$ (seven drops) is reached only at
 598 time $t = 750$ for $2\delta\theta_s = 14^\circ$. This slowing down is a direct consequence of the lowering of
 599 the speed of the drops in the presence of a contact angle hysteresis, as one can anticipate
 600 from the drop speed estimate (C 6).

601 To further understand the effect of the contact angle hysteresis on the drop merging
 602 process, we have performed a parametric study of the speed of a single sliding drop for
 603 different values of $2\delta\theta_s$ as the mass of the drop is varied. Figure 13 reports the result
 604 of this parametric study and shows a dramatic effect of the contact angle hysteresis on
 605 small drops, whose speed is significantly lowered. However, for large drops, this effect is

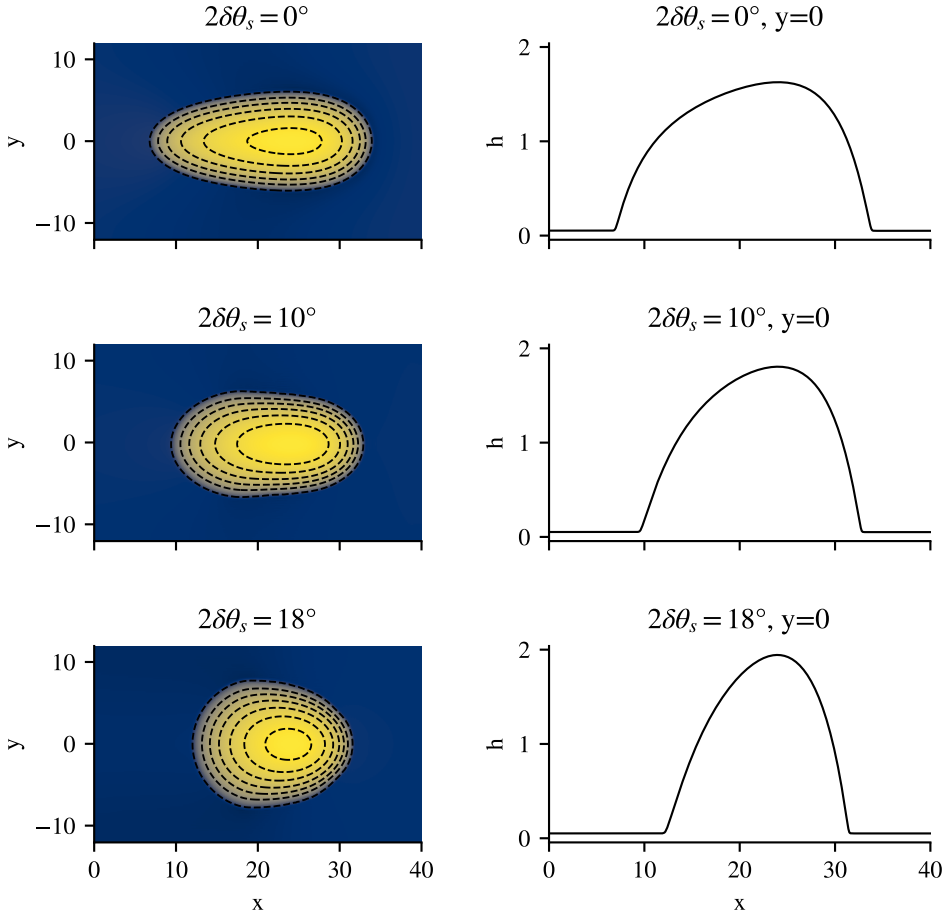


Figure 10: Snapshots of the free surface elevation at $t = 350$ in a domain of size $2.4 \text{ mm} \times 7.2 \text{ mm}$ with $N \times 3N = 310^4$ nodes for different hysteresis of the static contact angle $2\delta\theta_s = 0^\circ$, 10° and 18° .

606 mitigated by their size. As a consequence, the slowing down of the coarsening dynamics
 607 by the contact angle hysteresis is more efficient in the early stages of the coalescence
 608 process.

609 4 Conclusion and perspectives

610 In this work, a mathematical and numerical framework has been developed to study
 611 the displacement and merging dynamics of sliding droplets under the action of a constant
 612 shear exerted by a gas flow. The mathematical development has been developed in
 613 Section 2. An augmented formulation has been implemented to model surface tension
 614 including correctly the full curvature of the free surface. Details can be found in [Bresch](#)
 615 *et al.* (2020). A set of shallow-water evolution equations for the film thickness h , the
 616 averaged velocity \mathbf{U} , the additional velocity \mathbf{W} and an enstrophy tensor Φ , have been
 617 obtained. The enstrophy Φ accounts for the deviation of the velocity profile from the
 618 constant velocity distribution that is usually assumed in the Saint-Venant equations and

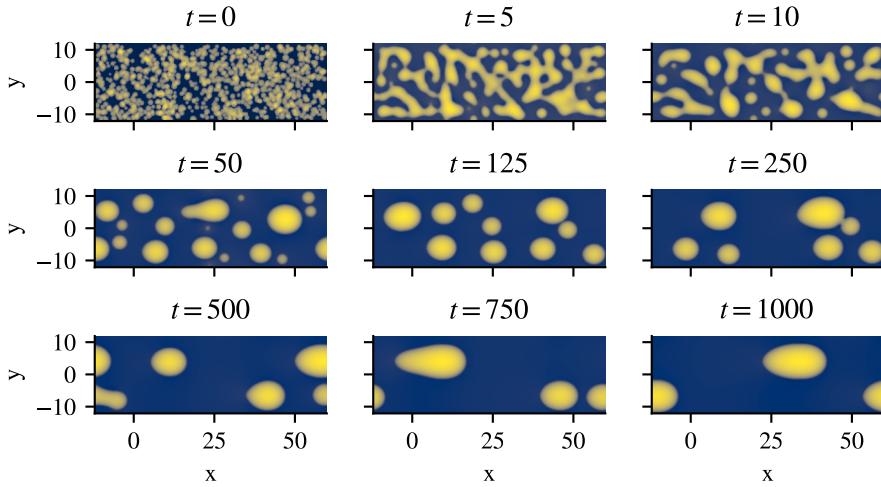


Figure 11: Snapshots of the free surface elevation at different times in a domain of size $24 \text{ mm} \times 8 \text{ mm}$ with $3N \times N = 2 \cdot 10^6$ nodes for a constant contact angle $\theta_s = 30^\circ$.

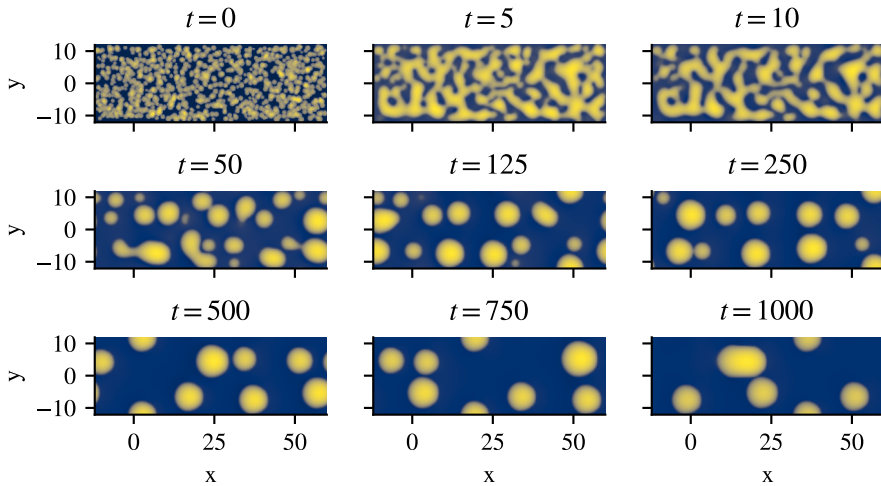


Figure 12: Snapshots of the free surface elevation at different times in a domain of size $24 \text{ mm} \times 8 \text{ mm}$ with $3N \times N = 2 \cdot 10^6$ nodes for a hysteresis $2\delta\theta_s = 14^\circ$ ($\theta_r = 23^\circ$ and $\theta_a = 37^\circ$).

619 is not verified for viscous flows at low Reynolds numbers. The formulation is consistent
 620 with the long-wave expansion of the basic equations, remains hyperbolic and conservative.
 621 Finally, our model has been completed with a disjoining pressure formulation that is able
 622 to account for the hysteresis of the static contact angle. In this formulation, the advancing
 623 or receding nature of the contact line is assessed by the accumulation or reduction of mass
 624 of the droplet at the contact line (sign of $\text{div}(h\mathbf{U})$). Section 3 is devoted to an in-house
 625 2D numerical solver implementing the proposed model. This code is written in Julia and
 626 uses the method of line. We discuss the contact angle hysteresis and provide simulation of
 627 single droplet as well as dynamics of coarsening. The derivation of the enstrophy equation
 628 and a discussion on drop speed is given in Appendix A.

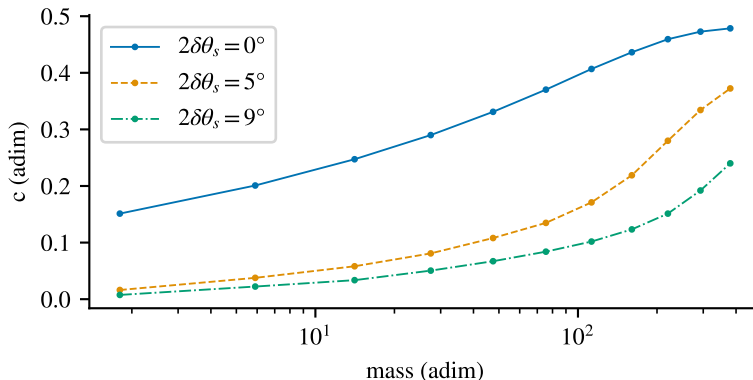


Figure 13: droplet terminal velocity in a domain of size 24 mm×8 mm with $3N \times N = 210^6$ nodes for hysteresis $2\delta\theta_s = 0^\circ$, $2\delta\theta_s = 5^\circ$ and $2\delta\theta_s = 9^\circ$ according to the droplet initial mass.

629 Simulations of sliding water droplets have been performed with periodic boundary
 630 conditions in a domain of limited size. Our simulations show a transition of the shape of the
 631 sliding droplets from a tear-drop shape to a bullet shape with a round back and an
 632 ogival front as the hysteresis of the contact angle is raised. Simulations of the coarsening
 633 dynamics of the drop demonstrate a slowdown of the drops and a delay in the sequence
 634 of coalescence of the drops due to the contact angle hysteresis.

635 We have limited ourselves to consider only a constant shear stress at the free surface.
 636 However, several studies suggest a retroaction of the droplet geometry on the gas flow
 637 (Pozrikidis 1997; Ding & Spelt 2008; Sellier *et al.* 2019). Razzaghi & Amirfazli (2019) thus
 638 showed that the shedding of a sessile droplet by an airflow is affected by the presence of
 639 other droplets nearby. Hooshanginejad & Lee (2017) revealed that this interaction results
 640 from the modification of the pressure field induced by the wake of the first droplet on
 641 the second one. It is therefore important to extend the present liquid-side formulation to
 642 a two-phase flow one for which the gas motion is resolved (Lavalle *et al.* 2017). This will
 643 be investigated in a subsequent work.

644 **Acknowledgments** We acknowledge support by the Fraise project, grant ANR-16-
 645 CE06-0011 of the French National Research Agency (ANR), and by the H2020 project:
 646 optiwind through Horizon 2020/clean sky2 (call H2020-CS2-CFP06-2017-01) with Saint
 647 Gobain and LOCIE-LAMA.

648 **Declaration of Interests.** The authors report no conflict of interest.

649

650 A Derivation of the enstrophy equation

651 Denoting $\mathbf{u} = (u, v)^T$ and $\boldsymbol{\tau}_{sh} = (\tau_{xz}, \tau_{yz})^T$, the equations (2.19)–(2.20) can be written

$$\frac{\partial \mathbf{u}}{\partial t} + \mathbf{div}(\mathbf{u} \otimes \mathbf{u}) + \frac{\partial w \mathbf{u}}{\partial z} = -\kappa \mathbf{grad} p + \frac{1}{\varepsilon Re} \frac{\partial \boldsymbol{\tau}_{sh}}{\partial z} + O(\varepsilon). \quad (\text{A1})$$

Forming $\mathbf{u} \otimes (\text{A } 1) + (\text{A } 1) \otimes \mathbf{u}$ gives

$$\frac{\partial \mathbf{u} \otimes \mathbf{u}}{\partial t} + \text{div}(\mathbf{u} \otimes \mathbf{u} \otimes \mathbf{u}) + \frac{\partial w \mathbf{u} \otimes \mathbf{u}}{\partial z} = \frac{1}{\varepsilon Re} \left(\mathbf{u} \otimes \frac{\partial \boldsymbol{\tau}_{sh}}{\partial z} + \frac{\partial \boldsymbol{\tau}_{sh}}{\partial z} \otimes \mathbf{u} \right) - \kappa \mathbf{u} \otimes \mathbf{grad} p - \kappa \mathbf{grad} p \otimes \mathbf{u} \quad (\text{A } 2)$$

Since $\langle \mathbf{u}' \otimes \mathbf{u}' \otimes \mathbf{u}' \rangle = O(\varepsilon)$ (it is equal to zero at order zero), depth averaging this equation over the depth leads to

$$\begin{aligned} \frac{\partial}{\partial t} [h(\mathbf{U} \otimes \mathbf{U} + h^2 \boldsymbol{\varphi})] + \text{div}(h\mathbf{U} \otimes \mathbf{U} \otimes \mathbf{U} + h^3 \mathbf{U} \otimes \boldsymbol{\varphi} + h^3 \boldsymbol{\varphi} \otimes \mathbf{U}) \\ + [\text{div}(h^3 \mathbf{U} \otimes \boldsymbol{\varphi})]^\text{T} = \frac{1}{\varepsilon Re} \left[\frac{3}{2} (\mathbf{U} \otimes \boldsymbol{\tau}_e + \boldsymbol{\tau}_e \otimes \mathbf{U}) - \frac{6}{h} \mathbf{U} \otimes \mathbf{U} \right] \\ + \kappa h (\mathbf{U} \otimes \mathbf{grad} K + \mathbf{grad} K \otimes \mathbf{U}) + O(\varepsilon) \quad (\text{A } 3) \end{aligned}$$

Forming $\mathbf{U} \otimes (\text{2.45}) + (\text{2.45}) \otimes \mathbf{U}$ leads to

$$\begin{aligned} \frac{\partial}{\partial t} (h\mathbf{U} \otimes \mathbf{U}) + \text{div}(h\mathbf{U} \otimes \mathbf{U} \otimes \mathbf{U} + h^3 \mathbf{U} \otimes \boldsymbol{\varphi}) + [\text{div}(h^3 \mathbf{U} \otimes \boldsymbol{\varphi})]^\text{T} \\ - h^3 \mathbf{grad} \mathbf{U} \cdot \boldsymbol{\varphi} - h^3 \boldsymbol{\varphi} \cdot (\mathbf{grad} \mathbf{U})^\text{T} = \frac{1}{\varepsilon Re} \left[\frac{3}{2} (\mathbf{U} \otimes \boldsymbol{\tau}_e + \boldsymbol{\tau}_e \otimes \mathbf{U}) - \frac{6}{h} \mathbf{U} \otimes \mathbf{U} \right] \\ + \kappa h (\mathbf{U} \otimes \mathbf{grad} K + \mathbf{grad} K \otimes \mathbf{U}) + O(\varepsilon) \quad (\text{A } 4) \end{aligned}$$

652 The difference between (A 3) and (A 4) gives

$$\frac{\partial h \boldsymbol{\Phi}}{\partial t} + \text{div}(h \boldsymbol{\Phi} \otimes \mathbf{U}) - 2h(\text{div} \mathbf{U}) \boldsymbol{\Phi} + \mathbf{grad} \mathbf{U} \cdot h \boldsymbol{\Phi} + h \boldsymbol{\Phi} \cdot (\mathbf{grad} \mathbf{U})^\text{T} = O(\varepsilon) \quad (\text{A } 5)$$

653 Because of (2.47), this equation can be consistently written as (2.48) where a relaxation

654 term is added at the right-hand side with an arbitrary constant β which should be chosen

655 large so that $\boldsymbol{\varphi}$ relaxes toward its equilibrium value.

656 B Dimensional equations

657 In dimensional form, the equations of the model (2.57) can be written

$$\frac{\partial h}{\partial t} + \text{div}(h\mathbf{U}) = 0, \quad (\text{B } 1)$$

$$\begin{aligned} \frac{\partial h \mathbf{U}}{\partial t} + \text{div}(h\mathbf{U} \otimes \mathbf{U} + h^3 \boldsymbol{\Phi}) = \frac{3}{2} \frac{\boldsymbol{\tau}_e}{\rho} - 3\nu \frac{\mathbf{U}}{h} + h \mathbf{grad} \Pi \\ + \text{div} \left[h (\mathbf{grad}(\mathbf{f}_1 \cdot \mathbf{W}))^\text{T} \right] - \mathbf{grad}(\mathbf{f}_2 \cdot \mathbf{W}), \quad (\text{B } 2) \end{aligned}$$

658

$$\frac{\partial h \mathbf{W}}{\partial t} + \text{div}(h \mathbf{W} \otimes \mathbf{U}) = -\mathbf{f}_1 \cdot \text{div} \left[h (\mathbf{grad} \mathbf{U})^\text{T} \right] - \mathbf{f}_2 \text{div} \mathbf{U}, \quad (\text{B } 3)$$

$$\begin{aligned} \frac{\partial h \boldsymbol{\Phi}}{\partial t} + \text{div}(h \boldsymbol{\Phi} \otimes \mathbf{U}) - 2h(\text{div} \mathbf{U}) \boldsymbol{\Phi} + \mathbf{grad} \mathbf{U} \cdot h \boldsymbol{\Phi} + h \boldsymbol{\Phi} \cdot (\mathbf{grad} \mathbf{U})^\text{T} \\ = -B \frac{\nu}{h} \left[\boldsymbol{\Phi} - \frac{\mathbf{U} \otimes \mathbf{U}}{3h^2} + \frac{1}{12h^2} \left(\mathbf{U} \otimes \mathbf{U} - \frac{h^2}{4\rho^2 \nu^2} \boldsymbol{\tau}_e \otimes \boldsymbol{\tau}_e \right) \right], \quad (\text{B } 4) \end{aligned}$$

659 where the expression of the disjoining pressure is

$$\Pi = \frac{(n-1)(m-1)}{n-m} \frac{\gamma}{\rho} \frac{1-\cos\theta_s}{h^*} \left[\left(\frac{h^*}{h} \right)^n - \left(\frac{h^*}{h} \right)^m \right] \quad (\text{B5})$$

660 and where the second-order tensor \mathbf{f}_1 is given by

$$\mathbf{f}_1(h, \mathbf{W}) = \sqrt{\frac{\gamma h}{\rho}} h \left(1 + \frac{\rho h}{4\gamma} \|\mathbf{W}\|^2 \right)^{-1/2} \left[\mathbf{I} - \frac{\rho h}{4\gamma} \left(1 + \frac{\rho h}{2\gamma} \|\mathbf{W}\|^2 \right)^{-1} \mathbf{W} \otimes \mathbf{W} \right] \quad (\text{B6})$$

661 and the vector \mathbf{f}_2 by

$$\mathbf{f}_2(h, \mathbf{W}) = \frac{h\mathbf{W}}{2} \left(1 + \frac{\rho h}{2\gamma} \|\mathbf{W}\|^2 \right)^{-1}. \quad (\text{B7})$$

662 In the 1D-case, these equations become

$$\frac{\partial h}{\partial t} + \frac{\partial hU}{\partial x} = 0, \quad (\text{B8})$$

663

$$\frac{\partial hU}{\partial t} + \frac{\partial}{\partial x} (hU^2 + h^3\varphi) = \frac{3}{2} \frac{\tau_e}{\rho} - 3\nu \frac{U}{h} + h \frac{\partial \Pi}{\partial x} + \frac{\partial}{\partial x} \left(h \frac{\partial f_1 W}{\partial x} \right) - \frac{\partial f_2 W}{\partial x}, \quad (\text{B9})$$

664

$$\frac{\partial hW}{\partial t} + \frac{\partial hUW}{\partial x} = -f_1 \frac{\partial}{\partial x} \left(h \frac{\partial U}{\partial x} \right) - f_2 \frac{\partial U}{\partial x}, \quad (\text{B10})$$

665

$$\frac{\partial h\varphi}{\partial t} + \frac{\partial hU\varphi}{\partial x} = -B \frac{\nu}{h} \left(\varphi - \frac{U^2}{4h^2} - \frac{\tau_e^2}{48\rho^2\nu^2} \right), \quad (\text{B11})$$

666 where Π is given by (B5) and where

$$f_1(h, W) = \sqrt{\frac{\gamma h}{\rho}} \frac{1}{\sqrt{1 + \frac{h\rho}{4\gamma} W^2}} \left(1 - \frac{h\rho}{4\gamma} \frac{W^2}{1 + \frac{h\rho}{2\gamma} W^2} \right), \quad (\text{B12})$$

667

$$f_2(h, W) = \frac{hW}{2} \frac{1}{1 + \frac{h\rho}{2\gamma} W^2}. \quad (\text{B13})$$

668 C Droplet speed

669 In this section, we consider a two-dimensional drop moving at a constant shape and
 670 speed and try to determine its speed. We develop arguments similar to the ones proposed
 671 by Gennes *et al.* (1990), Schwartz & Eley (1998) and Lallement (2019). The drop is
 672 entrained by the gas shear stress and arrested by the viscous wall shear stress and the
 673 adhesion force, a constant speed is achieved when the three forces balance each other, or
 674 equivalently when the sum of their work cancels.

675 The dissipative work of the wall shear stress read in that case

$$dW_\mu = \int \left[\frac{2\mu U^2}{h} dt \right] dx \quad (\text{C1})$$

676 whereas the work of the shear stress reads

$$dW_s = \int [\tau_e U dt] dx = \tau_e U L dt \quad (\text{C2})$$

677 where L stands for the length of the drop. Finally, the work of the surface tension is

$$dW_{\text{cap}} = \gamma (\cos \theta_a - \cos \theta_r) U dt. \quad (\text{C } 3)$$

678 Writing that the work of the dissipative wall shear stress is compensated by the work of
679 the shear stress at the free surface and surface tension, i.e. $-dW_\mu + dW_s + dW_{\text{cap}} = 0$
680 gives an expression for the drop velocity U . Since the dissipative work is a function of
681 h^{-1} , it is dominated by the viscous stresses in the vicinity of the contact line

$$\int \frac{dx}{h} = \int \frac{dx}{dh} \frac{dh}{h} \approx \left(\frac{1}{\tan(\theta_{da})} + \frac{1}{\tan(\theta_{dr})} \right) \log \left(\frac{H}{h^*} \right) \quad (\text{C } 4)$$

682 H refers to the drop height at which the advancing and receding dynamical contact angles
683 θ_{da} and θ_{dr} are measured. We thus obtain the estimate

$$dW_\mu \approx 2\mu U^2 dt \left(\frac{1}{\tan(\theta_{da})} + \frac{1}{\tan(\theta_{dr})} \right) \log \left(\frac{H}{h^*} \right) \quad (\text{C } 5)$$

684 Therefore the drop velocity can be approximated by

$$U \approx \frac{1}{2\mu [(\tan \theta_{da})^{-1} + (\tan \theta_{dr})^{-1}] \log \left(\frac{H}{h^*} \right)} [\tau_e L - \gamma (\cos \theta_r - \cos \theta_a)] \quad (\text{C } 6)$$

685 We thus expect a reduction of the speed of the drop in presence of a hysteresis of the
686 static contact angle. This effect shall be more important for small drops than for large
687 drops as it depends on the ratio $\gamma/(\tau_e L)$. We also expect that the inverse of the drop
688 speed is a linear function of the logarithm of the precursor film thickness h^* .

REFERENCES

- 689 AHMED, G., SELIER, M., JEREMY, M. & TAYLOR, M. 2014 Modeling the effects of contact
690 angle hysteresis on the sliding of droplets down inclined surfaces. *European Journal of*
691 *Mechanics - B/Fluids* **48**, 218–230.
- 692 BERTOZZI, ANDREA L & PUGH, MARY 1994 The lubrication approximation for thin viscous
693 films: the moving contact line with a porous media cut-off of van der Waals interactions.
694 *Nonlinearity* **7** (6), 1535.
- 695 BRACKBILL, J. U., KOTHE, D. B. & ZEMACH, C. 1992 A continuum method for modeling
696 surface tension. *J. Comput. Phys.* **100** (2), 335–354.
- 697 BRANDON, S., WACHS, A. & MAMUR, A. 1997 Simulated contact angle hysteresis of a three-
698 dimensional drop on a chemically heterogeneous surface: a numerical example. *J. Colloid*
699 *Interface Sci.* **191**, 110–116.
- 700 BRESCH, D., CELLIER, N., COUDERC, F., GISCLON, M., NOBLE, P., RICHARD, G. L., RUYER-
701 QUIL, C. & VILA, J.-P. 2020 Augmented skew-symmetric system for shallow-water system
702 with surface tension allowing large gradient of density. *Journal of Computational Physics*
703 **419**, 109670.
- 704 BRESCH, DIDIER, COLIN, MATHIEU, MSHEIK, KHAWLA, NOBLE, PASCAL & SONG, XI 2019 Bd
705 entropy and Bernis–Friedman entropy. *Comptes Rendus Mathematique* **357** (1), 1–6.
- 706 BRESCH, D., COUDERC, F., NOBLE, P. & VILA, J.-P. 2016 A generalization of the quantum
707 Bohm identity: Hyperbolic CFL condition for Euler–Korteweg equations. *Comptes Rendus*
708 *Mathematique* **354** (1), 39–43.
- 709 BRESCH, DIDIER & NOBLE, PASCAL 2007 Mathematical justification of a shallow water model.
710 *Methods and Applications of Analysis* **14** (2), 87–118.
- 711 CHURAEV, N.V. & SOBOLEV, V.D. 1995 Prediction of contact angles on the basis of the
712 Frumkin-Derjaguin approach. *Advances in Colloid and Interface Science* **61**, 1–16.
- 713 DERJAGUIN, B.V. 1940 *Zh. Fiz. Khim.* **14**, 137.
- 714 DIEZ, J. A., KONDIC L. & BERTOZZI, A. 2000 Global models for moving contact lines. *Phys.*
715 *Rev. E* **63**, 011208.

- 716** DING, H. & SPELT, P. D. M. 2008 Onset of motion of a three-dimensional droplet on a wall in
717 shear flow at moderate reynolds numbers. *Journal of Fluid Mechanics* **599**, 341–362.
- 718** DUSSAN, E. B. 1979 On the spreading of liquids on solid surfaces: Static and
719 dynamic contact lines. *Annual Review of Fluid Mechanics* **11** (1), 371–400, arXiv:
720 <https://doi.org/10.1146/annurev.fl.11.010179.002103>.
- 721** ESPÍN, LEONARDO & KUMAR, SATISH 2017 Droplet wetting transitions on inclined substrates
722 in the presence of external shear and substrate permeability. *Phys. Rev. Fluids* **2**, 014004.
- 723** FAN, J., WILSON, M.C.T. & KAPUR, N. 2011 Displacement of liquid droplets on a surface by
724 a shearing air flow. *Journal of Colloid and Interface Science* **356** (1), 286–292.
- 725** DE GENNES, P. G. 1985 Wetting: statics and dynamics. *Rev. Mod. Phys.* **57**, 827–863.
- 726** GENNES, P. G. DE, HUA, X. & LEVINSON, P. 1990 Dynamics of wetting: local contact angles.
727 *Journal of Fluid Mechanics* **212**, 55–63.
- 728** GODUNOV, S. K. & BOHACHEVSKY, I. 1959 Finite difference method for numerical computation
729 of discontinuous solutions of the equations of fluid dynamics. *Matematičeskij sbornik*
730 **47(89)** (3), 271–306.
- 731** GOSSET, A. 2017 Prediction of rivulet transition in anti-icing applications. In *7th Eur. Conf.*
732 *Aeronautics and Aerospace Sci.*, p. 482. EUCASS.
- 733** GOTTLIEB, S., SHU, C.-W. & TADMOR, E. 2001 Strong stability-preserving high-
734 order time discretization methods. *SIAM Review* **43** (1), 89–112, arXiv:
735 <https://doi.org/10.1137/S003614450036757X>.
- 736** HALEY, PATRICK J. & MIKSYS, MICHAEL J. 1991 The effect of the contact line on droplet
737 spreading. *Journal of Fluid Mechanics* **223**, 57–81.
- 738** HOOSHANGINEJAD, ALIREZA & LEE, SUNGYON 2017 Droplet depinning in a wake. *Phys. Rev.*
739 *Fluids* **2**, 031601.
- 740** LALLEMENT, JULIEN 2019 Modélisation et simulation numérique d'écoulements de films minces
741 avec effet de mouillage partiel. Theses, Université de Toulouse.
- 742** LALLEMENT, J., TRONTIN, P., LAURENT, C. & VILLEDIEU, P. 2018 A shallow water type
743 model to describe the dynamic of thin partially wetting films for the simulation of anti-
744 icing systems. In *AIAA Aviation Forum, 2018 Atmospheric and Space Environments*
745 *Conference*, p. 3012. AIAA, June 25–29, 2018, Atlanta, Georgia.
- 746** LAN, H., FRIEDRICH, M., ARMALY, B. F. & DRALLMEIER, J. A. 2008 Simulation and
747 measurement of 3d shear-driven thin liquid film flow in a duct. *Int. J. Heat and Fluid*
748 *Flow* **29**, 449–459.
- 749** LAVALLE, GIANLUCA, VILA, JEAN-PAUL, LUCQUIAUD, MATHIEU & VALLURI, PRASHANT 2017
750 Ultraefficient reduced model for countercurrent two-layer flows. *Phys. Rev. Fluids* **2**,
751 014001.
- 752** LUCHINI, PAOLO & CHARRU, FRANÇOIS 2019 On the large difference between benjamin's and
753 hanratty's formulations of perturbed flow over uneven terrain. *Journal of Fluid Mechanics*
754 **871**, 534–561.
- 755** MAHÉ, M., VIGNES-ADLER, M, ROUSSEAU, A, JACQUIN, C.G & ADLER, P.M 1988 Adhesion
756 of droplets on a solid wall and detachment by a shear flow: I. pure systems. *Journal of*
757 *Colloid and Interface Science* **126** (1), 314–328.
- 758** MEREDITH, K. V., HEATHER, A., DE VRIES, J. & XIN, Y. 2011 A numerical model for partially-
759 wetted flow of thin liquid films. In *Computational Methods in Multiphase Flows VI*, pp.
760 239–250.
- 761** MILNE, A. J. B. & AMIRFAZLI, A. 2009 Drop shedding by shear flow for hydrophilic to
762 superhydrophobic surfaces. *Langmuir* **25** (24), 14155–14164.
- 763** MOGHATERNEJAD, S., JADIDI M. ESMAIL N. & DOLATABADI, A. 2014 Shear driven rivulet
764 dynamics on surfaces with various wettabilities. In *Proc. Int. Mech. Engng Congress and*
765 *Exposition IMECE2014*, p. 38665. ASME, Montreal, Quebec, Canada.
- 766** MOGHATERNEJAD, S., JADIDI, M., ESMAIL, N. & DOLATABADI, A. 2016 Shear-driven droplet
767 coalescence and rivulet formation. *Proc. Inst. Mech. Engineers, Part C : J. Mech. Engng*
768 *Si.* **230** (5), 793–803.
- 769** NOBLE, P. & VILA, J.P. 2014 Stability theory for difference approximations of Euler–Korteweg
770 equations and application to thin film flows. *SIAM Journal on Numerical Analysis* **52** (6),
771 2770–2791.

- 772 ORON, ALEXANDER, DAVIS, STEPHEN H. & BANKOFF, S. GEORGE 1997 Long-scale evolution
773 of thin liquid films. *Rev. Mod. Phys.* **69**, 931–980.
- 774 POPESCU, M N, OSHANIN, G, DIETRICH, S & CAZABAT, A-M 2012 Precursor films in wetting
775 phenomena. *Journal of Physics: Condensed Matter* **24** (24), 243102.
- 776 POZRIKIDIS, C 1997 Shear flow over a protuberance on a plane wall. *Journal of Engineering*
777 *Mathematics* **31** (1), 29–42.
- 778 RAZZAGHI, A. & AMIRFAZLI, A. 2019 Shedding of a pair of sessile droplets. *Int. J. Multiphase*
779 *Flow* **110**, 59–68.
- 780 REN, WEIQING & E, WEINAN 2007 Boundary conditions for the moving contact line
781 problem. *Physics of Fluids* **19** (2), 022101, arXiv: [https://pubs.aip.org/aip/pof/article-
782 pdf/doi/10.1063/1.2646754/15636165/022101_1_online.pdf](https://pubs.aip.org/aip/pof/article-pdf/doi/10.1063/1.2646754/15636165/022101_1_online.pdf).
- 783 RICHARD, G. L., DURAN, A. & FABRÈGES, B. 2019a A new model of shoaling and breaking
784 waves. part 2. run-up and two-dimensional waves. *J. Fluid Mech.* **867**, 146–194.
- 785 RICHARD, G. L., GISCLON, M, RUYER-QUIL, C & VILA, J.-P. 2019b Optimization of consistent
786 two-equation models for thin film flows. *European Journal of Mechanics-B/Fluids* **76**, 7–
787 25.
- 788 SAVVA, N. & KALLIADASIS, S. 2009 Two-dimensional droplet spreading over topographical
789 substrates. *Physics of Fluids* **21** (9), 092102.
- 790 SCHWARTZ, L. W. & ELEY, R. R. 1998 Simulation of droplet motion on low-energy and
791 heterogeneous surfaces. *J. Colloid Interface Sci.* **202**, 173–188.
- 792 SELLIER, M., GRAYSON, J. W., RENBAUM-WOLFF, L., SONG, M. & BERTRAM, A. K.
793 2015 Estimating the viscosity of a highly viscous liquid droplet through the
794 relaxation time of a dry spot. *Journal of Rheology* **59** (3), 733–750, arXiv:
795 https://pubs.aip.org/sor/jor/article-pdf/59/3/733/16014235/733_1_online.pdf.
- 796 SELLIER, M., TAYLOR, J., BERTRAM, A. K. & MANDIN, P. 2019 Models for the bead mobility
797 technique: A droplet-based viscometer. *Aerosol Science and Technology* **53** (7), 749–759.
- 798 SIBLEY, D.N., NOLD, A., SAVVA, N. & KALLIADASIS, S. 2015 A comparison of slip, disjoining
799 pressure, and interface formation models for contact line motion through asymptotic
800 analysis of thin two-dimensional droplet spreading. *J. Eng. Math.* **94**, 19–41.
- 801 TESHUKOV, V. M. 2007 Gas-dynamic analogy for vortex free-boundary flows. *J. Appl. Mech.*
802 *Tech. Phys.* **48**, 303–309.
- 803 ZHANG, K., WEI, T. & HU, H. 2015 An experimental investigation on the surface water
804 transport process over an airfoil by using a digital image projection technique. *Exp. Fluids*
805 **56**, 173.
- 806 ZHANG, K., ROTHMAYER A. P. & HU, H. 2016 An experimental investigation on the dynamic
807 water runback process over an airfoil surface pertinent to aircraft icing phenomena. In
808 *8th AIAA Atmospheric and Space Environments Conference*, p. 3138. AIAA, 13–17 June
809 Washington D.C.
- 810 ZHAO, Y. & MARSHALL, J.S. 2006 Dynamics of driven liquid films on heterogeneous surfaces.
811 *J. Fluid Mech.* **559**, 355–378.
- 812